Four-fluid MHD Simulations of the Plasma and Neutral Gas Environment of Comet 67P/Churyumov-Gerasimenko Near Perihelion

Zhenguang Huang[1], Gabor Toth[1], Tamas I. Gombosi[1], Xianzhe Jia[1], Martin Rubin[2], Nicolas Fougere[1], Valeriy Tenishev[1], Michael R. Combi[1], Andre Bieler[1], Kenneth C. Hansen[1], Yinsi Shou[1], Kathrin Altwegg[2]

[1]Department of Climate and Space Sciences and Engineering, University of Michigan, Ann Arbor, MI 48109

[2]Physikalisches Institut, University of Bern, Bern, Switzerland

This is the author manuscript accepted for publication and has undergone full peer review but has not been through the copyediting, typesetting, pagination and proofreading process, which may lead to differences between this version and the Version of Record. Please cite this article as doi: 10.1002/2015JA022333

Key Points.

- A 3D coupled neutral gas and multi-fluid plasma model for a comet is developed.
- Formation of nightside magnetic pileup region is found.
- Nucleus directed plasma flow inside the nightside reconnection region is found.

Abstract.

The neutral and plasma environment is critical in understanding the interaction of the solar wind and comet 67P/Churyumov-Gerasimenko (CG), the target of the European Space Agency's Rosetta mission. To serve this need and support the Rosetta mission, we have developed a 3-D four-fluid model, which is based on BATS-R-US (Block-Adaptive Tree Solarwind Roe-type Upwind Scheme) within SWMF (Space Weather Modeling Framework) that solves the governing multi-fluid MHD equations and the Euler equations for the neutral gas fluid. These equations describe the behavior and interactions of the cometary heavy ions, the solar wind protons, the electrons, and the neutrals. This model incorporates different mass loading processes, including photo-ionization and electron impact ionization, charge exchange, dissociative ion-electron recombination, and collisional interactions between different fluids. We simulated the plasma and neutral gas environment near perihelion in three different cases: an idealized comet with a spherical body and uniform neutral gas outflow, an idealized comet with a spherical body and illumination driven neutral gas outflow, and comet CG with a realistic shape model and illumination driven neutral gas outflow. We compared the results of the three cases and showed that the simulations with illumination driven neutral gas outflow have magnetic reconnection, a magnetic pile-up

region and nucleus directed plasma flow inside the nightside reconnection region, which have not been reported in the literature.

1. Introduction

The goal of the Rosetta mission [*Glassmeier et al.*, 2007] is to study the physical and chemical properties of a comet. The spacecraft has rendezvoused with comet 67P/Churyumov-Gerasimenko (CG) in August 2014 and will observe the comet until 2016. As the comet approaches the Sun, the interaction region of the comet with the solar wind undergoes significant changes. *Hansen et al.* [2007] simulated the plasma environment of comet CG for different phases of the Rosetta mission with a single fluid magnetohydrodynamic (MHD) model and a hybrid particle model. They showed that the single fluid MHD model has certain limitations because the single fluid equations treat the solar wind protons and the cometary heavy ions as a single combined fluid. Without separating the velocities between different ion fluids, the single fluid MHD model cannot reproduce effects arising from the gyration of the cometary ions and the deflection of the solar wind protons. *Rubin et al.* [2014a, b] developed a multi-fluid MHD model, which treats the solar wind protons and the cometary ions as separate fluids. They have shown that, with multi-fluid equations, the model is able to produce effects arising from the gyration of the cometary pick-up ions, which is in good agreement with the 3D Hybrid AIKEF model [*Koenders et al.*, 2015]. On the other hand, *Rubin et al.* [2014a, b] applied a spherically symmetric neutral gas background from the analytical Haser model [*Haser*, 1957] in their simulations, which is a crude approximation. Recent neutral gas simulations by *Bieler et al.* [2015] have shown that the shape of the nucleus and the solar illumination have a strong impact on the neutral gas outflow, which results in a non-spherical and time-dependent neutral gas distribution. As a consequence, the cometary heavy ions are

expected to have a non-spherical distribution because they are produced by the ionization of the neutral gas. *Goldstein et al.* [2015] and *Edberg et al.* [2015] observed that the plasma density varies with the comet nucleus rotation. It is, therefore, critical to apply the realistic neutral gas distribution in the multi-fluid simulations to understand its impact on the plasma environment of comet CG, especially in the inner coma region where the neutral gas distribution is significantly different from the spherical symmetry assumed in the Haser model.

It is nearly impossible to propose an analytical solution for the neutral gas due to the complex nucleus shape and illumination coupled with the comet's rotation. So the neutral gas has to be one of the simulated fluids in the model if we want to study the plasma environment around irregularly shaped comet CG. In this paper, we present a multi-fluid model which treats the cometary neutral gas, the cometary heavy ions, the solar wind protons, and the neutralizing electrons as separate fluids. An inner boundary with an arbitrary shape is also implemented to incorporate the realistic nucleus in the simulation. In this paper, we mainly focus on the inner coma region, where the distribution of the plasma is significantly affected by the complex outgassing pattern from the nucleus.

2. Model Equations

In this section, we describe the multi-fluid equations for the cometary neutral gas, the cometary heavy ions, the solar wind protons, and the electrons. *Najib et al.* [2011] and *Dong et al.* [2014] have simulated the solar wind interactions with Mars with multi-fluid equations, while *Rubin et al.* [2014a, b] have studied the plasma environment at two different comets. *Benna and Mahaffy* [2007] developed a 3D multi-fluid model to study a Halley-class coma using the solar-wind conditions of the Giotto flyby of Halley in 1986.

Rubin et al. [2015a] have also applied a multi-fluid model to simulate the plasma interaction with Jupiter's moon, Europa. We use ρ, p, $\mathbf{u}$, γ, and I to denote the mass density, pressure, velocity vector, the specific heat ratio, and the identity matrix, respectively. The subscripts n, s, and e correspond to the cometary neutral gas, the ions (either the cometary heavy ions or the solar wind protons), and the electrons, respectively.

The first set of equations is the hydrodynamic equations for the cometary neutral gas

$$\begin{aligned}
&\frac{\partial \rho_n}{\partial t} + \nabla \cdot (\rho_n \mathbf{u_n}) = \frac{\delta \rho_n}{\delta t} \\
&\frac{\partial \rho_n \mathbf{u_n}}{\partial t} + \nabla \cdot (\rho_n \mathbf{u_n} \mathbf{u_n} + p_n I) = \frac{\delta \rho_n \mathbf{u_n}}{\delta t} \\
&\frac{\partial p_n}{\partial t} + \nabla \cdot (p_n \mathbf{u_n}) + (\gamma_n - 1) p_n (\nabla \cdot \mathbf{u_n}) = \frac{\delta p_n}{\delta t}
\end{aligned} \tag{1}$$

consisting of the continuity equation, the momentum equation, and the pressure equation. The right hand sides describe the source terms, including the loss due to photo-ionization and the addition due to recombination. However, in this study, we focus on the near nucleus environment, i.e. much smaller than the ionization scale length, which is about 1.67×10^6 km if we consider the photo-ionization frequency as $6 \cdot 10^{-7}$ s^{-1} and the cometary neutral gas velocity as 1 km/s. The source and the loss terms are very small near the comet, so we set the right hand sides to zero. We will consider these terms in future work when we study the large scale structures extending to large cometocentric distances.

The equations for the cometary heavy ions, the solar wind protons, and the electrons are the multi-ion MHD equations:

$$\begin{aligned}
&\frac{\partial \rho_s}{\partial t} + \nabla \cdot (\rho_s \mathbf{u_s}) = \frac{\delta \rho_s}{\delta t} \\
&\frac{\partial \rho_s \mathbf{u_s}}{\partial t} + \nabla \cdot (\rho_s \mathbf{u_s} \mathbf{u_s} + p_s \mathrm{I}) \\
&\qquad - Z_s e \frac{\rho_s}{m_s} (\mathbf{E} + \mathbf{u_s} \times \mathbf{B}) = \frac{\delta \rho_s \mathbf{u_s}}{\delta t} \\
&\frac{\partial p_s}{\partial t} + \nabla \cdot (p_s \mathbf{u_s}) + (\gamma_s - 1) p_s (\nabla \cdot \mathbf{u_s}) = \frac{\delta p_s}{\delta t} \\
&\frac{\partial p_e}{\partial t} + \nabla \cdot (p_e \mathbf{u_s}) + (\gamma_e - 1) p_e (\nabla \cdot \mathbf{u_e}) = \frac{\delta p_e}{\delta t}
\end{aligned} \tag{2}$$

The first three equations are the continuity, the momentum, and the pressure equations for the ions (either the cometary heavy ions or solar wind protons). Z and e denote the ion charge state and the unit charge, respectively. $\mathbf{E}$ is the electric field vector while $\mathbf{B}$ is

the magnetic field vector. u_+ is the charge averaged ion velocity, which can be expressed as $u_+ = \frac{\sum_{s=ions} Z_s n_s \mathbf{u_s}}{n_e}$ (n_e is the electron number density). We assume charge neutrality, so the electron number density can be obtained from $n_e = \sum_{s=ions} Z_s n_s$. The fourth equation in Equation 2 is the electron pressure equation.

The source terms for plasma fluids are incorporated into the right hand sides of Equation 2. $\frac{\delta \rho_s}{\delta t}$ are the source terms for the continuity equation, which include the photo-ionization from the neutral gas, the charge-exchange between the neutral gas and the ion species s and the dissociative ion-electron recombination. $\frac{\delta \rho_s \mathbf{u_s}}{\delta t}$ are the source terms for the momentum equation, which include the newly ionized ions implanted at the neutral bulk velocity, the charge-exchange between the neutral gas and the ions, the elastic collisions between the ions and other particles (the neutrals, other ions and the electrons), and the dissociative ion-electron recombination. The ion pressure source terms $\frac{\delta p_s}{\delta t}$ include photo-ionization, electron impact ionization, charge exchange, recombination, and elastic collisions with other particles. The electron pressure source term $\frac{\delta p_e}{\delta t}$ contains photo-ionization, electron impact ionization, charge exchange, recombination, elastic collisions with other particles, and inelastic collisions with neutral water molecules. Detailed discussion of the source terms can be found in *Rubin et al.* [2014a, b]. We briefly mention some of the coefficients here. The photo-ionization frequency depends on the heliocentric distance of the comet and will be provided in Section 3. The ion-neutral charge exchange rate for both cometary heavy ions and solar wind protons is $1.7 \cdot 10^{-15}$ [$\mathrm{m^3 s^{-1}}$], which is obtained from *Gombosi et al.* [1996]. The elastic collision rates are listed in Table 1. The dissociative ion-electron recombination rates are taken from *Schunk and Nagy* [2009]. The

value for the cometary heavy ion is given by

$$\alpha = \begin{cases} 1.57 \cdot 10^{-11}(T_e)^{-0.569} & \text{for} \quad T_e < 800\,\text{K} \\ 4.73 \cdot 10^{-11}(T_e)^{-0.74} & \text{for} \quad 800\,\text{K} < T_e < 4000\,\text{K} \\ 1.03 \cdot 10^{-9}(T_e)^{-1.11} & \text{for} \quad T_e > 4000\,\text{K} \end{cases} \tag{3}$$

in the units of $[\text{m}^3 s^{-1}]$ while it is $4.8 \cdot 10^{-18}(\frac{250}{T_e})^{0.7}$ $[\text{m}^3 s^{-1}]$ for the solar wind protons. The excessive energy added to the electron from the photo-ionization is 12.0 eV, which is taken from *Huebner et al.* [1992], while the energy lost due to electron impact ionization is 12.6 eV, which is obtained from *Haynes* [2013]. The inelastic collisions between electrons and neutral water molecules are an efficient way to cool the electrons in the inner coma region and the cooling rate is provided by *Gombosi* [2015] in the unit of [eV cm^3 s^{-1}]:

$$L_e = 4 \cdot 10^{-9}[1 - \exp(-\frac{k(T_e - T_n)}{0.033\,\text{eV}})] + A[0.415 - \exp(-\frac{kT_e - 0.10\,\text{eV}}{0.10\,\text{eV}})] \tag{4}$$

where $A = 0$ for $kT_e \leq 0.188\,\text{eV}$ and $A = 6.5 \cdot 10^{-9}$ for $kT_e > 0.188\,\text{eV}$.

The electric field vector can be derived from the electron momentum equation neglecting the inertial terms:

$$\mathbf{E} = -\mathbf{u_e} \times \mathbf{B} - \frac{1}{n_e e}\nabla p_e \tag{5}$$

where $\mathbf{u_e} = \mathbf{u}_+ + \mathbf{u_H}$ is the electron velocity with the Hall velocity $\mathbf{u_H} = -\frac{\mathbf{j}}{n_e e}$, and $\mathbf{j} = (\mathbf{1}/\mu_\mathbf{0})\nabla \times \mathbf{B}$ is the current density.

If we substitute the electric field into the ion momentum equation, we then get the modified ion momentum equation:

$$\frac{\partial \rho_s \mathbf{u_s}}{\partial t} + \nabla \cdot (\rho_s \mathbf{u_s} \mathbf{u_s} + p_s \mathrm{I}) - Z_s n_s (\mathbf{u_s} - \mathbf{u}_+) \times \mathbf{B} - \frac{Z_s n_s}{n_e e}(\mathbf{j} \times \mathbf{B} - \nabla p_e) + Z_s n_s = \frac{\delta \rho_s \mathbf{u_s}}{\delta t} \tag{6}$$

It is important to point out that the term $Z_s n_s(\mathbf{u_s} - \mathbf{u}_+)$ provides the force that makes different species gyrate around the charge-average ion velocity $\mathbf{u}_+$, which can explain the gyration of the cometary pick-up ions and the deflection of the solar wind protons. We will discuss this in more detail in the following section.

Finally, the magnetic field is obtained from Faraday's law. In our comet simulations, we neglect the Hall velocity and the electron pressure gradient term in the induction equation, so it becomes

$$\frac{\partial \mathbf{B}}{\partial t} = \nabla \times (\mathbf{u}_+ \times \mathbf{B}) \tag{7}$$

The Hall velocity term, which allows the ions and electrons to move at different velocities, is important when the current is significant, for example, the magnetopause [*Mozer et al.*, 2002] and the tail region [*Ma and Bhattacharjee*, 1998]. In the present study, we ignore the Hall velocity term. A future study will include the Hall term to see the Hall effect in comet simulations.

3. Simulation Setup

The BATS-R-US (Block-Adaptive Tree Solarwind Roe-type Upwind Scheme) code [*Powell et al.*, 1999; *Tóth et al.*, 2012] can solve the multi-fluid equations described in the previous section on a 3D block adaptive grid that can resolve different length scales. Because the boundary conditions for the cometary ions and the solar wind is not easy to define near the comet, we need to simulate a large domain of about one million kilometers in all directions, such that the upstream boundary condition is the undisturbed solar wind. On the other hand, the nucleus of comet CG is about 2 km in equivalent radius, so the smallest cell in the simulation has to be small enough to capture the complex shape of the nucleus. The computational domain in this study extends from -10^6 to $+10^6$ km in the x direction, and from -0.5×10^6 to 0.5×10^6 km in both y and z directions. The smallest cell is about 0.12 km near the comet while the largest cell is about 31,250 km far away from the nucleus, with 18 levels of refinements increasing the resolution by a factor of two at every level. There are about 9000 blocks with 4.56 million cells. The Sun is at

the +x direction and the solar wind moves along the -x direction. The comet nucleus is properly rotated so that the Sun illuminates it at a realistic angle. The interplanetary field points in the y direction.

The cometary neutral gas is taken to be water as H_2O is the major neutral gas observed by ROSINA onboard Rosetta, even though CO_2 could be more abundant for some time periods [*Hässig et al.*, 2015]. The cometary heavy ions then are H_2O^+, which are produced by the photo-ionization and charge exchange of H_2O molecules. The specific heat ratio can be expressed by $\gamma = \frac{f+2}{f}$, where f is the degrees of freedom of a gas molecule. H_2O and H_2O^+ possess 3 translational and 3 rotational degrees of freedom, so the specific heat ratio is $\frac{4}{3}$ for them. The solar wind protons and electrons contain 3 translational degrees of freedom, so their specific heat ratio is $\frac{5}{3}$. At this stage we neglect ion-neutral reactions, in particular the formation of H_3O^+ which was the dominant ion in the near nucleus coma of comet 1P/Halley. Also for CG, H_3O^+ is at times dominating [*Fuselier et al.*, 2015] and we will investigate this in our future work. At large distance, the water molecules are dissociated into H and O, then the composition of the cometary ions is more complex. *Shou et al.* [2015] applied a multi-species MHD model with an imposed neutral gas background that accounts for the separated H_2O, OH, O, H, CO and CO_2 contributions, and they showed that the details of the ion composition (H_2O^+, H_3O^+, OH^+ and O^+) are affected outside 50,000 km from the nucleus. In this work, we neglect this process.

The cometary neutral gas source is driven by the solar illumination. The boundary conditions for the neutral gas fluid is described in detail in *Bieler et al.* [2015]. The inner boundary condition is applied at the cell faces (we define this as the comet surface

in the simulation, which separates the grid cells inside and outside of the comet) such that the neutral density, the velocity, and the temperature match the mass and energy flux of a half-Maxwellian particle distribution. The particle flux and temperature are approximated by $F = F_{\min}+(F_{\max}-F_{\min})\cos\theta$ and $T = \max[T_{\min}, T_{\max}+\Delta T(1-1/\cos\theta)]$, where $F_{\min}$, $F_{\max}$, $T_{\min}$, $T_{\max}$, ΔT, θ are the minimum flux, the maximum flux, the minimum temperature, the maximum temperature, a fitting parameter, and the solar zenith angle, respectively. At the outer boundary, the neutral gas can freely leave the simulation domain.

The boundary conditions for the plasma fluids are not trivial. The inner boundary conditions are specified at the comet surface for each fluid. If the plasma flow (either the cometary heavy ions or the solar wind protons) is moving into the body then it is set to be floating (or zero gradient), which means the comet can absorb the ions. When the flow is leaving out of the surface then the velocity for the particular fluid is set to zero while the mass density and pressure are set to a low value so that the comet surface is not a significant source for ions. The outer boundary conditions are specified at the edge of the simulation domain. The cometary ions can freely leave the simulation box at the outer boundary in all directions; while the upstream boundary condition for the solar wind protons is the undisturbed solar wind and the solar wind can freely leave the simulation domain on all other sides.

We focus on steady-state snapshots of the simulation, even though the code can run in time-dependent mode. Steady state simulations can provide useful information like the bow shock location, the size and the shape of the diamagnetic cavity at reasonable computational cost. In steady-state simulations, the comet does not show any time varia-

tions. The steady state assumption is reasonable near the comet (within several hundred kilometers of the nucleus) for the same illumination direction from the following simple consideration. Since the neutral gas outflow velocity is about 1 km/s, the time scale of the variations within several hundred kilometers of the comet is about several hundred seconds, which is very short compared with the comet rotation period (about 12 hours). On the other hand, steady-state simulations can take advantage of the local time stepping technique, in which case the grid cell advances at its local stable time-step. In addition, the plasma source terms are evaluated with a point-implicit algorithm, so the stiffness of these terms do not limit the time step [*Tóth et al.*, 2012]. This algorithm can significantly speed up the convergence toward a steady state. At larger scales, where the time scales become comparable to the rotation period, time dependent simulations are needed because the environment is not determined by a fixed illumination direction. Time dependent simulations are also needed when the solar wind is very dynamic. We will carry out time-dependent simulations in future studies.

The local time step in the simulation is controlled by the maximum speed among the sound wave speed of the neutral gas and the fast magnetosonic wave speed of the plasma. As the fast magnetosonic wave speed is much larger than the neutral gas bulk and sound speeds, we would waste lots of computational resources if we ran the neutral gas and the plasma fluids together. To save CPU time, we first run a neutral gas only simulation to get a steady-state solution for the neutral gas background and then run the coupled neutral gas and the multi-fluid plasma together to obtain the final steady-state results.

We simulate the near coma neutral gas and plasma environment for three cases:

1. An idealized comet with a spherical body and uniform neutral gas outflow.

2. An idealized comet with a spherical body and the neutral gas outflow is driven by solar illumination.

3. Comet 67P/Churyumov-Gerasimenko with a realistic shape model SHAP5.1 [*Preusker et al.*, 2015] and the neutral gas outflow is driven by solar illumination.

Case 1 is a model validation study to be compared to *Rubin et al.* [2015b], who simulated the multi-fluid plasma environment with a Haser neutral gas background of comet CG at different heliocentric distances. Case 1 can also be compared with *Koenders et al.* [2015], who simulated comet CG at 1.3 AU with a hybrid code. Case 2 improves the model by considering a non-uniform neutral gas outflow driven by solar illumination. Case 3 investigates the effect of using a realistic nucleus shape in the simulation. The Sun position is at latitude $-34°$ and longitude $157°$ in the cometary coordinate system, corresponding to the time at 06:00:00 UT 2015-07-16 .

As the neutral gas outflow is illumination driven, we need to adjust the local flux production rate at the comet surface to keep the total gas production rate the same for all three cases. In our study, we apply the total gas production rate as $Q = 8 \cdot 10^{27}$ /s [*Hansen et al.*, 2016], which is higher than the total gas production rate ($Q = 5 \cdot 10^{27}$ /s) that *Rubin et al.* [2015b] and *Koenders et al.* [2015] used. Because the neutral gas outflow is uniform for Case 1, so $F_{\min} = F_{\max}$ and $T_{\min} = T_{\max}$. We set $T_{\min} = T_{\max} = 170.7$ K. For Cases 2 and 3, the ratio of $F_{\min}$ and $F_{\max}$ and the values of $T_{\min}$ and $T_{\max}$ are derived from *Davidsson et al.* [2007] and *Tenishev et al.* [2008]. At 1.3 AU, the ratio between $T_{\max}$ and $T_{\min}$ is 73 approximately. To adjust the local neutral gas production rate, we apply an arbitrary $F_{\max}$ with $F_{\min} = F_{\max}/73$ to run the neutral gas only model until the solution reaches its steady state. We then obtain the total gas production rate Q_{model}

by integrating the neutral gas flux through a spherical surface at $r = 3\,\mathrm{km}$ and calculate the ratio $R = Q/Q_{\mathrm{model}}$. Because the neutral gas solution depends linearly on F_{min} and F_{max}, we can simply multiply them with ratio R to obtain the desired production rate Q. *Gombosi et al.* [1986] showed that the neutral gas temperature drops to a very low value with fluid simulations due to the rapid cooling when the neutral gas expands from the comet's surface into the coma. *Rubin et al.* [2014a] set the neutral gas temperature to 100 K in their simulations, so we also set the minimum temperature of the neutral gas in this study to 100 K in case the neutral gas temperature drops below that. The minimum temperature of the cometary ions, the solar wind protons and the electrons is also set to 100 K. We have also performed simulations with different minimum neutral gas temperatures. The overall structures are very similar, but the exact locations of the plasma boundaries are slightly different, which is expected as the minimum neutral gas temperature can change the neutral gas velocity. In the inner coma region, the cometary ion velocity is strongly coupled with the neutral gas velocity. The major impact of different minimum neutral gas temperatures is the configuration of the current sheet. Since the reconnection process cannot be completely captured with a fluid model, the solution in this region is not expected to be perfect in any case.

The parameters for the local flux production rate and the temperature are listed in Table 2, while the input parameters are listed in Table 3. Simulation results and discussion are presented in the next section.

4. Simulation Results and Discussion

Case 1 studies an idealized comet with a spherical body and uniform neutral gas outflow, whose neutral gas solution is very close to the Haser model [*Haser*, 1957]. The neutral gas

density in the Haser model can be described as $n_h = \frac{Q_h}{4\pi u_n |r|^2} e^{-\frac{|r| \cdot \nu_{io}}{u_n}}$, where Q_h is the total gas production rate, r is the distance from the comet center, u_n is the outflow velocity, and ν_{io} is the ionization frequency, respectively. The major differences to our model are that the outflow velocity is not a constant and there is no loss due to photo-ionization at this time in our simulation. As we are interested in the inner coma environment, the loss terms to the neutral gas fluid can be neglected. They are important when we study the environment far away from the comet. The cometary neutral gas density for Case 1 and the Haser model (where we substitute $Q_h = 8 \cdot 10^{27}\,\mathrm{s}^{-1}$, $u_n = 1\,\mathrm{km/s}$ and $\nu_{io} = 6 \cdot 10^{-7}\,\mathrm{s}^{-1}$ in the Haser model equation to obtain the neutral gas density) is shown in the upper panel in Figure 1. The lower panel plots the cometary neutral gas velocity for Case 1 in the same range. It can be seen that the cometary neutral gas density for Case 1 is very close to what is obtained from the Haser model, especially within 200 km of the nucleus. At larger distances, the Haser model has a higher density than Case 1, which is due to the fact that the cometary neutral gas velocity for Case 1 is higher than the Haser model (see the lower panel).

Case 2 simulates an idealized comet with a spherical body and non-uniform neutral gas outflow which is driven by solar illumination. This simulation is a better approximation than Case 1 because the solar illumination is taken into account and it is the driver of the neutral gas outflow. As we will show later in this section, the neutral gas solution shows a strong asymmetry between the dayside and nightside, with larger neutral gas density in the dayside (see Figure 3 and 4 and related discussion in Section 4.1). The asymmetry in the neutral gas solution leads to a very different cometary heavy ion distribution because the cometary heavy ions come from the neutrals through photo-ionization and charge

exchange. Case 3 investigates how the non-spherical nucleus changes the near coma environment. To perform this study, we incorporated a realistic shape model SHAP5.1 [*Preusker et al.*, 2015] of Comet 67P/Churyumov-Gerasimenko.

4.1. Neutral Gas

Figure 2 shows the neutral gas distribution in the y=0 plane in the full simulation domain. The top, middle and bottom panels represent Cases 1, 2 and 3, respectively. As expected, the neutral gas distribution is spherically symmetric in Case 1 because the neutral gas outflow is uniformly distributed on the sphere. Case 2 shows a strong neutral gas outflow on the dayside because the flow is solar illumination driven, while the distribution is still symmetric around the x axis. The realistic CG simulation (Case 3) is represented by the bottom panel where we consider both the shape and the solar illumination, and no symmetries can be found.

Figure 3 shows the neutral gas solutions in a 2D plane within 400 km of the comet center. The left three panels show the H_2O number density in the y=0 plane for the three cases, while the right three panels present the solution in the z=0 plane. It is obvious that the neutral gas solution in the top panels have a symmetric distribution as expected from a spherical body with uniform outflow. When the neutral gas outflow is solar illumination driven, the neutral gas solution has a strong asymmetry between dayside and nightside, as shown in the middle panels. The neutral gas solution becomes more asymmetic when the real shape of comet CG is taken into account, as indicated in the bottom panels. Similar behaviors can be seen in Figure 4, which plots the neutral gas velocity distribution in a 2D plane within 400 km of the comet center in a similar manner. The neutral gas velocities obtained from the MHD model are consistent with what are obtained by *Bieler et al.*

[2015] with a pure neutral gas fluid model, even though the values are larger than the expansion velocity of about 0.68 km/s, which is reported by *Gulkis et al.* [2015].

The cometary neutral gas temperature is 100 K everywhere. The reason is that due to the rapid cooling, the cometary neutral gas temperature drops to a small value when the neutral gas expands from the comet's surface into the coma [*Gombosi et al.*, 1986]. As we set the minimum temperature of the neutral gas to 100 K, the neutral gas could not drop below 100 K. We also rerun Case 3 with the minimum neutral gas temperature set to 50 K or 150 K, and we found that the structures look similar with minor differences.

4.2. Cometary Heavy Ions

Figure 5 plots the cometary heavy ion (H_2O^+) distribution in the y=0 plane in the full simulation domain. The three cases do not show significant differences on the large scale. Because far away from the comet, the cometary heavy ion density drops to a small value ($< 10^{-2}$ cm^{-3}), the cometary ion flow is mainly controlled by the solar wind flow. *Rubin et al.* [2014b] observed the gyration of the cometary heavy ion (see Figure 1 in their paper) at a heliocentric distance 2.7 AU from the Sun in their simulations. Beside fluid simulations, *Bagdonat and Motschmann* [2002] also observed the gyration with their hybrid simulation for comet Wirtanen. The gyration comes from the term $Z_s n_s(\mathbf{u_s} - \mathbf{u}_+)$ in Equation 6. As the cometary ions and the solar wind protons are coupled together behind the bow shock (which will be discussed later, see Figure 9), the velocity difference between the cometary ions and the solar wind protons is small. Due to the small difference between the two ion fluid velocities and a stronger magnetic field at 1.3 AU, the gyration effect is reduced and not visible in our simulations. A multi-fluid simulation of comet

CG at 1.3 AU provided by *Rubin et al.* [2015b] also confirmed that the gyration is not visible at this heliocentric distance.

Figure 6 shows the H_2O^+ distribution within 400 km of the nucleus, where the cometary heavy ion distribution shows significant differences due to the different neutral gas distributions (see Figure 3). In the shadow of the nucleus, where the photo-ionization rate drops to zero, the cometary ion density drops to small values, as indicated in the figure. Another noticeable feature is a density enhancement region at around +50 km for Case 1, and +120 km for Cases 2 and 3 (see Figure 7) on the dayside in all three cases. This density enhancement is the so-called recombination layer, which has been observed previously by the Giotto mission [*Balsiger et al.*, 1986; *Goldstein et al.*, 1989] and numerically simulated by *Cravens* [1989] and *Gombosi et al.* [1996]. This recombination layer lies between the inner shock, which slows down the supersonic cometary ion flow to subsonic flow, and the contact surface that the solar wind protons can not penetrate. Figure 7 shows that the recombination layer is inside the peak of the solar wind proton density, which is formed by the pile-up of the solar wind protons in front of the contact surface, indicating that the recombination layer is inside the contact surface. With respect to comet CG, *Koenders et al.* [2015] reported a recombination layer in-between 25 km and 45 km away from the nucleus when they simulated the plasma interaction region of the comet at 1.3 AU, which is in good agreement with our Case 1 result. *Rubin et al.* [2015b] applied a multi-fluid code to study comet CG and found a recombination layer in-between 32 km and 42 km.

4.3. Bow Shock Position

Figure 8 shows density of the solar wind protons in the y=0 plane in the full simulation domain for all three cases. The three simulation cases do not show noticeable differences at large scale. Again, because the solar wind protons and cometary ions have similar velocities behind the bow shock, no large scale gyration can be observed in the figure. A bow shock is found at around 6,000 km in Case 1 and about 10,000 km in both Case 2 and Case 3. We summarize the distance of the bow shock along the +x axis in Table 4. The shock position can be seen more clearly in Figure 9, which shows the H^+ density in a smaller region. *Galeev et al.* [1985] obtained an analytical approximation of the bow shock distance by considering mass loading and charge-exchange in the continuity equation, the momentum equation and the pressure equation:

$$R_{bs} = \frac{m_i}{m_p} \frac{QI_0}{4\pi u_n n_{sw} u_{sw} [(\hat{\rho}\hat{u})_c - 1]} \tag{8}$$

where m_i, m_p, n_{sw}, u_{sw}, I_0, u_n, and Q are the mass of the cometary heavy ion, the mass of the solar wind proton, the solar wind number density, the solar wind speed, the ionization frequency, the neutral gas outflow velocities, and the total neutral gas production rate, respectively. $\hat{\rho}\hat{u}$ is the contaminated solar wind flow parameter, which is equal to a critical value of $(\hat{\rho}\hat{u})_c = 1.185$ for a $M = 2$ shock from their numerical simulations. *Koenders et al.* [2013] suggested that the radius of the nucleus has a small impact on the bow shock position and replaced $((\hat{\rho}\hat{u})_c - 1)$ in Equation 8 with $((\hat{\rho}\hat{u})_c - 1 + A)$, where $A = \frac{m_i}{m_p} \frac{QI_0}{4\pi u_n n_{sw} u_{sw} (u_{sw} \cdot I_0 + R_{nucleus})}$. They showed that A only has a tiny impact on the bow shock position, which only shifts the bow shock position by about 0.3% in their study. For the sake of simplicity, we applied Equation 8 to estimate the bow shock position. If we substitute $m_i = 18$ amu, $m_p = 1$ amu, $n_{sw} = 6\,\mathrm{cm}^{-3}$, $u_{sw} = 400$ km/s, $I_0 = 6 \cdot 10^{-7}\,\mathrm{s}^{-1}$,

$u_n = 1\,\mathrm{km/s}$, and $Q = 8 \cdot 10^{27}\,\mathrm{s}^{-1}$ into the equation, we obtain $R_{bs} \approx 15,000\,\mathrm{km/s}$, which is 50% to twice larger than the bow shock distances from the simulations. *Rubin et al.* [2015b] found a bow shock at around 3000 km in their simulation of comet CG near perihelion, which is about 40% closer than our Case 1 result. This is expected because they applied a lower neutral gas production rate as $5 \cdot 10^{27}\,\mathrm{s}^{-1}$ while we apply $8 \cdot 10^{27}\,\mathrm{s}^{-1}$, and they applied a Haser neutral gas background while the neutral gas fluid in Case 1 is different than the Haser model (see Figure 1).

4.4. Diamagnetic Cavity

Figure 10 shows the magnetic field magnitude in a 2D plane within 400 km of the nucleus. The left three panels show the magnetic field strength in the y=0 plane, while the right three panels show the magnetic field strength along with magnetic field traces in the z=0 plane for the three cases. In all cases, a diamagnetic cavity is found near the comet within 50 km to 100 km (see Figure 11), and a magnetic field pile-up region is formed in front of the cavity. We summarize the distance of the diamagnetic cavity along the +x axis in Table 4. The maximum magnetic field strength is about 72 nT in Case 1 and 60 nT in both Cases 2 and 3. *Koenders et al.* [2015] obtained a maximum magnetic field strength of 78 nT in their hybrid simulation, which is in good agreement with our Case 1 value.

As discussed by *Cravens* [1986], the diamagnetic cavity is inside the contact surface and a cometary contact surface is formed when the $\mathbf{j} \times \mathbf{B}$ force is balanced by the ion-neutral drag force. *Gombosi* [2015] provided an analytical approximation of the radius of the

contact surface:

$$R_{cs} = \sqrt{\frac{m_i}{m_p}\frac{k_{in}}{4\pi d_h n_{sw} u_{sw}^2}\sqrt{\frac{I_0}{4\pi\alpha u_n}}}Q^{3/4} \quad (9)$$

where m_i, m_p, k_{in}, d_h, n_{sw}, u_{sw}, I_0, u_n, Q are the mass of the cometary heavy ion, the mass of the solar wind proton, the ion-neutral charge transfer collision frequency, the heliocentric distance, the solar wind number density, the solar wind speed, the photo-ionization frequency, the neutral gas velocity, the total neutral gas production rate, respectively, and $\alpha = 1.21 \times 10^{-5}/\sqrt{T_e}\,\mathrm{cm}^3/\mathrm{s}$ is the dissociative ion-electron recombination frequency where T_e is the electron temperature in Kelvins. If we substitute $m_i = 18\,\mathrm{amu}$, $m_p = 1\,\mathrm{amu}$, $k_{in} = 1.1 \times 10^{-9}\,\mathrm{cm}^3/\mathrm{s}$, $d_h = 1.3\,\mathrm{AU}$, $n_{sw} = 6\,\mathrm{cm}^{-3}$, $u_{sw} = 400\,\mathrm{km/s}$, $I_0 = 6 \cdot 10^{-7}\,\mathrm{s}$, $u_n = 1\,\mathrm{km/s}$, $Q = 8 \cdot 10^{27}\,\mathrm{s}^{-1}$, and $T_e = 100\,\mathrm{K}$ into the equation, we then get $R_{cs} = 75.3\,\mathrm{km}$. The top left panel in Figure 11 shows that the diamagnetic cavity is at around 50 km on the dayside for Case 1, which can be compared with the analytical approximation because both assume a spherical body with uniform outflow. This simulation shows that the distance is about 35% smaller than the analytical expectation, which is not an unreasonable comparison if we consider that the analytical derivation relies on several simplifying assumptions. When we compare the three cases shown in Figure 10, we find that Case 1 and Case 2 have symmetric structures as the neutral gas background is symmetric in both cases and the ion gyro-motion effect is small and does not cause significant asymmetries. On the other hand, Case 3 shows significant asymmetry due to the shape and orientation of the nucleus.

Koenders et al. [2015] reported a diamagnetic cavity at around 25 km in their hybrid simulation of comet CG at 1.3 AU, while *Rubin et al.* [2015b] predicted the distance at around 32 km from their multi-fluid simulations. These two simulations provide good

agreement with our Case 1 result if we consider the situation that we apply a larger neutral gas production rate ($8 \cdot 10^{27}\,\mathrm{s}^{-1}$) then their simulations ($5 \cdot 10^{27}\,\mathrm{s}^{-1}$) and the differences in the neutral gas background. *Goetz et al.* [2016] observed the diamagnetic cavity of CG at around 170 km away from the nucleus, which is much further away than the predicted value (100 km) in Case 3. They suggested that instabilities propagating along the cavity boundary may be responsible for the unexpected large size of the diamagnetic cavity. Even though we do not observe instabilities in our simulations with fixed upstream solar wind boundary conditions, it is possible that with dynamic solar wind boundary conditions, instabilities can develop along the cavity boundary. This will require a time-dependent simulation and will be investigated in future studies.

4.5. Electron Temperature

Figure 12 plots the electron temperature along the x-axis. The electron temperature slightly increases (but is still coupled to the neutral gas temperature) along the Sun-comet line from the nucleus to the inner shock. The electrons cool slightly in the recombination layer. Then, the temperature starts to increase again beyond the recombination layer. A dramatic increase in the electron temperature is observed at around 80 km (Case 1) and 170 km (Cases 2 and 3), where the electron temperature decouples from the neutral temperature and therefore suppresses further ion-electron recombination. *Gombosi* [2015] provided an approximation of the electron-neutral decoupling distance as

$$R_{en} = \frac{208}{\sqrt{T_e}} \frac{Q}{10^{28}} \frac{R_n^2}{u_n} \tag{10}$$

where T_e, Q, u_n, and R_n are the electron temperature, the total gas production rate, the neutral gas velocity, and the comet radius, respectively. By substituting $T_e = 100\,\mathrm{K}$, $Q = 8 \cdot 10^{27}\,\mathrm{s}^{-1}$, $u_n = 1\,\mathrm{km/s}$, and $R_n = 2\,\mathrm{km}$, one can obtain a decoupling distance of

66.56 km, which compares well with Case 1 that assumes a spherically symmetric neutral gas distribution similar to the analytic assumption. The illumination driven cases (Cases 2 and 3), on the other hand, have much larger electron-neutron decoupling distances.

4.6. Cometary Ion Temperature

Figure 13 plots the cometary ion temperature along the x-axis. One can see that the cometary ion temperature is strongly coupled with the neutral gas temperature within the inner shock. The cometary ion temperature starts to increase in the recombination layer and beyond the recombination layer, and gradually increases to the solar wind ion temperature. This result is consistent with the simulation provided by *Cravens* [1989]. *Haerendel* [1987] and *Cravens* [1989] suggested that there are two processes associated with the increase of the cometary ion temperature. The first process is compressional heating associated with the contact surface, and it is dominant in the recombination layer. Beyond the recombination layer, the cometary ions are heated by frictional heating.

4.7. Reconnection in the Tail

Reconnection is a widely discussed phenomenon in the terrestrial magnetosphere [for example, *Birn et al.*, 2001] and planetary magnetospheres [e.g., *Paschmann et al.*, 2013]. *Russell et al.* [1986] proposed a reconnection model for comet tail disconnections, which is similar to the terrestrial substorm. They suggested that the encounter with an interplanetary shock or the decrease in solar wind Alfvén Mach number may trigger disconnection events in the comet tail region. We briefly discuss the reconnection that is observed in our simulations.

The top, middle and bottom panels in Figure 14 show the the magnetic field strength with the magnetic field vectors (left) and the cometary ion density with its velocity vectors (right) in the z=0 plane in the tail region for the three cases. It can be seen that the magnetic field changes its direction along the Sun - comet line, where the current sheet forms, in Cases 1 and 2, indicating occurrence of magnetic reconnections in this region. For Case 3, the current sheet is tilted because of the complex distribution of the cometary heavy ions due to the nucleus shape. In Cases 2 and 3, there is a magnetic pile-up region in the tail that isolates the diamagnetic cavity and the magnetotail current sheet. It is surprising to see that the cometary ion flow is very different between the three cases, especially between the uniform neutral gas outflow Case 1 and illumination driven neutral gas outflow Cases 2 and 3. In Case 1, the cometary heavy ions flow radially inside the diamagnetic cavity while the flow is controlled by the solar wind protons outside the recombination layer. In Case 2, the cometary heavy ions still flow radially inside the diamagnetic cavity and couple with the solar wind protons at large distances. However, within 200 km near the x-axis in the tail region, the cometary heavy ions flow towards the nucleus, which is not observed in Case 1. This nucleus directed plasma flow is associated with the magnetic reconnection in the tail region. When the nucleus directed plasma flow meets the the plasma flow moving radially outward, a cometary ion density pileup region is formed, which can explain the density peak observed in Figure 7. The compression between the two flows also results in a temperature increase in this region, which is also observed in Figure 12 and Figure 13. This compression is also responsible for the magnetic pile-up region discussed above. In Case 3, the cometary heavy ion flow is more complex, which is associated with the complex shape of the nucleus. Figure 15 shows the cometary

ion density with its velocity vectors in the y=0 plane. The top, middle, and bottom panels represent Cases 1, 2 and 3, respectively. Most of the features are similar to Figure 14.

Figure 16 shows the B_y component along the Sun-comet line for the three cases. It can be seen that the B_y component changes its direction at about 250 km in the tail direction, where the magnetic null point locates and the magnetic reconnection takes place. Figure 17 shows the X component of the cometary ion velocity V_x along the Sun-comet line. We can see that for Case 1, the cometary ion velocity does not change its sign, though a deceleration region of the flow can be found between 110 km and 160 km in the tail direction; whereas the flow changes its direction for Cases 2 and 3 at about 200 km. In a classical magnetic reconnection picture, the velocity changes its direction at the magnetic null point [*Parker*, 1957]. However, *Siscoe et al.* [2002] proposed a possible mode of the magnetic reconnection called "flow-through reconnection" or "FTR", in which case the plasma and magnetic field flow in opposite directions. Later Cluster observations have confirmed this reconnection mode [*Maynard et al.*, 2012]. This FTR seems to be the reconnection mode in our simulations. Case 1 represents an extreme case when the X component of the velocity does not change sign at all.

5. Summary and Conclusions

In this paper, we have presented a four fluid MHD model for a cometary plasma environment that includes the neutral gas, the cometary heavy ions, the solar wind protons, and the electrons. We investigated the plasma environment by performing three simulation runs: an idealized comet with a spherical body and uniform neutral gas outflow; an idealized comet with a spherical body and the neutral gas outflow driven by solar

illumination; comet 67P/Churyumov-Gerasimenko with nucleus shape SHAP5.1 and the neutral gas outflow driven by solar illumination as in Case 2.

Our simulation results show that the large scale plasma structures look similar among the three cases, though the bow shock distance for Case 1 is at about 6,000 km while it is located at around $10,000$ km in Cases 2 and 3. This difference can be explained by the fact that the neutral gas outflow is much stronger on the dayside for Cases 2 and 3. A stronger neutral gas outflow in effect can be mimicked by a higher total neutral gas production rate. If we again use Equation 8 to estimate the bow shock position, then a higher neutral gas production rate will push the bow show further away from the nucleus.

In the vicinity of the nucleus, the numerical model reproduces the main features predicted by analytic models: the inner shock, the recombination layer, the diamagnetic cavity and the contact surface. The locations of these features can be estimated by analytical formulas, and they provide values in reasonable agreement with the Case 1 simulation that assumes a spherically symmetric outflow for the neutrals. For the illumination driven simulations (Cases 2 and 3), the locations of these features are very anisotropic and different from the simple analytic estimates. The most distinct difference between Cases 2 and 3 is that in Case 3 the plasma structures are more realistic in the inner coma region, while Case 2 can only provide the general locations for these structures.

Our simulation results for the three cases show significant differences in the inner coma environment. When the solar illumination and/or the real shape of comet CG are taken into account, strong asymmetries can be observed in the neutral gas outflow, and the plasma environment changes accordingly in our simulations. We find that the neutral gas density, the cometary ion density, and the magnetic field magnitude have very different

distributions in the near coma region. Our simulations show some new features that have not been reported in the literature. We observe magnetic reconnection, a magnetic pile-up region and nucleus directed plasma flow inside the nightside reconnection region.

Bieler et al. [2015] have already performed numerical simulations from our neutral gas only model and compared with the observations from ROSINA onboard Rosetta and showed that our model results agree well with observations. It is essential to apply a realistic shape model in the simulation to have a detailed comparison between the simulation results and the plasma observations. It would be very interesting to compare the results from Case 3 with plasma observations onboard Rosetta. This will be done in a future study when the rotation of the nucleus and the time dependent solar illumination will be taken into account.

Acknowledgments.

We would like to thank the anonymous reviewers for comments that signicantly improved the manuscript.

This work was supported by the US Rosetta Project under JPL contract No.1266313.

The authors would like to thank the ROSINA team for supporting this research. The authors also thank the ESA Rosetta team for providing the opportunities to study this unique comet and their continuous support.

The authors would like to acknowledge high-performance computing resources: Yellowstone (ark:/85065/d7wd3xhc), provided by NCAR's Computational and Information Systems Laboratory, sponsored by the National Science Foundation; Pleiades, provided by the NASA Supercomputer Division at Ames; and Extreme Science and Engineering Dis-

covery Environment (XSEDE), supported by National Science Foundation grant number ACI-1053575

All the data in this manuscript can be obtained from the ICES website: http://ices.engin.umich.edu/.

References

Bagdonat, T., and U. Motschmann (2002), From a Weak to a Strong Comet - 3d Global Hybrid Simulation Studies, *Earth Moon and Planets*, *90*, 305–321, doi: 10.1023/A:1021578232282.

Balsiger, H., K. Altwegg, F. Buhler, J. Geiss, A. G. Ghielmetti, B. E. Goldstein, R. Goldstein, W. T. Huntress, W.-H. Ip, A. J. Lazarus, A. Meier, M. Neugebauer, U. Rettenmund, H. Rosenbauer, R. Schwenn, R. D. Sharp, E. G. Shelly, E. Ungstrup, and D. T. Young (1986), Ion composition and dynamics at comet Halley, *Nature*, *321*, 330–334, doi:10.1038/321330a0.

Benna, M., and P. Mahaffy (2007), Multi-fluid model of comet 1P/Halley, *Planet. Space Sci.*, *55*, 1031–1043, doi:10.1016/j.pss.2006.11.019.

Bieler, A., N. Fougere, G. Toth, V. Tenishev, M. Combi, T. Gombosi, K. Hansen, Z. Huang, X. Jia, K. Altwegg, P. Wurz, H. Balsiger, A. Jackel, L. Le Roy, S. Gasc, U. Calmonte, M. Rubin, C.-Y. Tzou, M. Hassig, S. Fuselier, et al. (2015), 3d kinetic and hydrodynamic modeling of the neutral coma of 67p/churyumov-gerasimenko, *Astron. Astrophys.,* , doi:10.1051/0004-6361/201526178.

Birn, J., J. F. Drake, M. A. Shay, B. N. Rogers, R. E. Denton, M. Hesse, M. Kuznetsova, Z. W. Ma, A. Bhattacharjee, A. Otto, and P. L. Pritchett (2001), Geospace Envi-

ronmental Modeling (GEM) magnetic reconnection challenge, *J. Geophys. Res.,* , *106*, 3715–3720, doi:10.1029/1999JA900449.

Cravens, T. E. (1986), The physics of the cometary contact surface, in *ESLAB Symposium on the Exploration of Halley's Comet*, *ESA Special Publication*, vol. 250, edited by B. Battrick, E. J. Rolfe, and R. Reinhard, pp. 241–246.

Cravens, T. E. (1989), A magnetohydrodynamical model of the inner coma of Comet Halley, *J. Geophys. Res.,* , *94*, 15,025–15,040, doi:10.1029/JA094iA11p15025.

Davidsson, B. J. R., P. J. Gutiérrez, and H. Rickman (2007), Nucleus properties of Comet 9P/Tempel 1 estimated from non-gravitational force modeling, *icarus*, *191*, 547–561, doi:10.1016/j.icarus.2006.07.031.

Dong, C., S. W. Bougher, Y. Ma, G. Toth, A. F. Nagy, and D. Najib (2014), Solar wind interaction with Mars upper atmosphere: Results from the one-way coupling between the multifluid MHD model and the MTGCM model, *Geophys. Res. Lett.,* , *41*, 2708–2715, doi:10.1002/2014GL059515.

Edberg, N. J. T., A. I. Eriksson, E. Odelstad, P. Henri, J.-P. Lebreton, S. Gasc, M. Rubin, M. André, R. Gill, E. P. G. Johansson, F. Johansson, E. Vigren, J. E. Wahlund, C. M. Carr, E. Cupido, K.-H. Glassmeier, R. Goldstein, C. Koenders, K. Mandt, Z. Nemeth, H. Nilsson, I. Richter, G. S. Wieser, K. Szego, and M. Volwerk (2015), Spatial distribution of low-energy plasma around comet 67P/CG from Rosetta measurements, *Geophys. Res. Lett.,* , *42*, 4263–4269, doi:10.1002/2015GL064233.

Fuselier, S. A., K. Altwegg, H. Balsiger, J. J. Berthelier, A. Bieler, C. Briois, T. W. Broiles, J. L. Burch, U. Calmonte, G. Cessateur, M. Combi, J. De Keyser, B. Fiethe, M. Galand, S. Gasc, T. I. Gombosi, H. Gunell, K. C. Hansen, M. Hässig, A. Jäckel,

A. Korth, L. Le Roy, U. Mall, K. E. Mandt, S. M. Petrinec, S. Raghuram, H. Rème, M. Rinaldi, M. Rubin, T. Sémon, K. J. Trattner, C.-Y. Tzou, E. Vigren, J. H. Waite, and P. Wurz (2015), ROSINA/DFMS and IES observations of 67P: Ion-neutral chemistry in the coma of a weakly outgassing comet, *Astron. Astrophys.,* , *583*, A2, doi:10.1051/0004-6361/201526210.

Galeev, A. A., T. E. Cravens, and T. I. Gombosi (1985), Solar wind stagnation near comets, *Astrophys. J.,* , *289*, 807–819, doi:10.1086/162945.

Glassmeier, K.-H., H. Boehnhardt, D. Koschny, E. Kührt, and I. Richter (2007), The Rosetta Mission: Flying Towards the Origin of the Solar System, *Space Sci. Rev.*, *128*, 1–21, doi:10.1007/s11214-006-9140-8.

Goetz, C., C. Koenders, I. Richter, et al. (2016), First detection of a diamagnetic cavity at comet 67p/churyumov-gerasimenko, *Astron. Astrophys.,* , in press.

Goldstein, B. E., K. Altwegg, H. Balsiger, S. A. Fuselier, and W.-H. Ip (1989), Observations of a shock and a recombination layer at the contact surface of Comet Halley, *J. Geophys. Res.,* , *94*, 17,251–17,257, doi:10.1029/JA094iA12p17251.

Goldstein, R., J. L. Burch, P. Mokashi, T. Broiles, K. Mandt, J. Hanley, T. Cravens, A. Rahmati, M. Samara, G. Clark, M. Hässig, and J. M. Webster (2015), The Rosetta Ion and Electron Sensor (IES) measurement of the development of pickup ions from comet 67P/Churyumov-Gerasimenko, *Geophys. Res. Lett.,* , *42*, 3093–3099, doi:10.1002/2015GL063939.

Gombosi, T. I. (2015), *Physics of Cometary Magnetospheres*, pp. 169–188, John Wiley & Sons, Inc, doi:10.1002/9781118842324.ch10.

Gombosi, T. I., A. F. Nagy, and T. E. Cravens (1986), Dust and neutral gas modeling of the inner atmospheres of comets, *Reviews of Geophysics*, *24*, 667–700, doi: 10.1029/RG024i003p00667.

Gombosi, T. I., D. L. De Zeeuw, R. M. Häberli, and K. G. Powell (1996), Three-dimensional multiscale MHD model of cometary plasma environments, *J. Geophys. Res.,* , *101*, 15,233–15,252, doi:10.1029/96JA01075.

Gulkis, S., M. Allen, P. von Allmen, G. Beaudin, N. Biver, D. Bockelée-Morvan, M. Choukroun, J. Crovisier, B. J. R. Davidsson, P. Encrenaz, T. Encrenaz, M. Frerking, P. Hartogh, M. Hofstadter, W.-H. Ip, M. Janssen, C. Jarchow, S. Keihm, S. Lee, E. Lellouch, C. Leyrat, L. Rezac, F. P. Schloerb, and T. Spilker (2015), Subsurface properties and early activity of comet 67P/Churyumov-Gerasimenko, *Science*, *347*(1), aaa0709, doi:10.1126/science.aaa0709.

Haerendel, G. (1987), Plasma transport near the magnetic cavity surrounding comet Halley, *Geophys. Res. Lett.,* , *14*, 673–676, doi:10.1029/GL014i007p00673.

Hansen, K. C., T. Bagdonat, U. Motschmann, C. Alexander, M. R. Combi, T. E. Cravens, T. I. Gombosi, Y.-D. Jia, and I. P. Robertson (2007), The Plasma Environment of Comet 67P/Churyumov-Gerasimenko Throughout the Rosetta Main Mission, *Space Sci. Rev.*, *128*, 133–166, doi:10.1007/s11214-006-9142-6.

Hansen, K. C., et al. (2016), Pre- and post-equinox rosina production rates calculated using a realistic empirical coma model derived from amps-dsmc simulations of comet 67p/churyumov-gerasimenko, in prepration.

Haser, L. (1957), Distribution d'intensité dans la tête d'une comète, *Bulletin de la Societe Royale des Sciences de Liege*, *43*, 740–750.

Hässig, M., K. Altwegg, H. Balsiger, A. Bar-Nun, J. J. Berthelier, A. Bieler, P. Bochsler, C. Briois, U. Calmonte, M. Combi, J. De Keyser, P. Eberhardt, B. Fiethe, S. A. Fuselier, M. Galand, S. Gasc, T. I. Gombosi, K. C. Hansen, A. Jäckel, H. U. Keller, E. Kopp, A. Korth, E. Kührt, L. Le Roy, U. Mall, B. Marty, O. Mousis, E. Neefs, T. Owen, H. Rème, M. Rubin, T. Sémon, C. Tornow, C.-Y. Tzou, J. H. Waite, and P. Wurz (2015), Time variability and heterogeneity in the coma of 67P/Churyumov-Gerasimenko, *Science*, *347*(1), aaa0276, doi:10.1126/science.aaa0276.

Haynes, W. M. (2013), *CRC Handbook of Chemistry and Physics, 94th Edition*, 2668 pp.

Huebner, W. F., J. J. Keady, and S. P. Lyon (1992), Solar photo rates for planetary atmospheres and atmospheric pollutants, *Astrophys. & Space Sci*, *195*, 1–289, doi: 10.1007/BF00644558.

Itikawa, Y. (1971), Effective collision frequency of electrons in atmospheric gases, *Planet. Space Sci.*, *19*, 993–1007, doi:10.1016/0032-0633(71)90149-8.

Koenders, C., K.-H. Glassmeier, I. Richter, U. Motschmann, and M. Rubin (2013), Revisiting cometary bow shock positions, *Planet. Space Sci.*, *87*, 85–95, doi: 10.1016/j.pss.2013.08.009.

Koenders, C., K.-H. Glassmeier, I. Richter, H. Ranocha, and U. Motschmann (2015), Dynamical features and spatial structures of the plasma interaction region of 67P/Churyumov-Gerasimenko and the solar wind, *Planet. Space Sci.*, *105*, 101–116, doi:10.1016/j.pss.2014.11.014.

Ma, Z. W., and A. Bhattacharjee (1998), Sudden enhancement and partial disruption of thin current sheets in the magnetotail due to Hall MHD effects, *Geophys. Res. Lett.,* , *25*, 3277–3280, doi:10.1029/98GL02432.

Maynard, N. C., C. J. Farrugia, W. J. Burke, D. M. Ober, F. S. Mozer, H. Rème, M. Dunlop, and K. D. Siebert (2012), Cluster observations of the dusk flank magnetopause near the sash: Ion dynamics and flow-through reconnection, *Journal of Geophysical Research (Space Physics)*, *117*, A10201, doi:10.1029/2012JA017703.

Mozer, F. S., S. D. Bale, and T. D. Phan (2002), Evidence of Diffusion Regions at a Subsolar Magnetopause Crossing, *Physical Review Letters*, *89*(1), 015002, doi:10.1103/PhysRevLett.89.015002.

Najib, D., A. F. Nagy, G. Tóth, and Y. Ma (2011), Three-dimensional, multifluid, high spatial resolution MHD model studies of the solar wind interaction with Mars, *Journal of Geophysical Research (Space Physics)*, *116*, A05204, doi:10.1029/2010JA016272.

Parker, E. N. (1957), Sweet's Mechanism for Merging Magnetic Fields in Conducting Fluids, *J. Geophys. Res.,* , *62*, 509–520, doi:10.1029/JZ062i004p00509.

Paschmann, G., M. Øieroset, and T. Phan (2013), In-Situ Observations of Reconnection in Space, *Space Sci. Rev.*, *178*, 385–417, doi:10.1007/s11214-012-9957-2.

Powell, K. G., P. L. Roe, T. J. Linde, T. I. Gombosi, and D. L. de Zeeuw (1999), A Solution-Adaptive Upwind Scheme for Ideal Magnetohydrodynamics, *Journal of Computational Physics*, *154*, 284–309, doi:10.1006/jcph.1999.6299.

Preusker, F., F. Scholten, K.-D. Matz, T. Roatsch, K. Willner, S. F. Hviid, J. Knollenberg, L. Jorda, P. J. Gutiérrez, E. Kührt, S. Mottola, M. F. A'Hearn, N. Thomas, H. Sierks, C. Barbieri, P. Lamy, R. Rodrigo, D. Koschny, H. Rickman, H. U. Keller, J. Agarwal, M. A. Barucci, J.-L. Bertaux, I. Bertini, G. Cremonese, V. Da Deppo, B. Davidsson, S. Debei, M. De Cecco, S. Fornasier, M. Fulle, O. Groussin, C. Güttler, W.-H. Ip, J. R. Kramm, M. Küppers, L. M. Lara, M. Lazzarin, J. J. Lopez Moreno, F. Marzari,

H. Michalik, G. Naletto, N. Oklay, C. Tubiana, and J.-B. Vincent (2015), Shape model, reference system definition, and cartographic mapping standards for comet 67P/Churyumov-Gerasimenko - Stereo-photogrammetric analysis of Rosetta/OSIRIS image data, *Astron. Astrophys.*, , *583*, A33, doi:10.1051/0004-6361/201526349.

Rubin, M., M. R. Combi, L. K. S. Daldorff, T. I. Gombosi, K. C. Hansen, Y. Shou, V. M. Tenishev, G. Tóth, B. van der Holst, and K. Altwegg (2014a), Comet 1P/Halley Multifluid MHD Model for the Giotto Fly-by, *Astrophys. J.*, , *781*, 86, doi:10.1088/0004-637X/781/2/86.

Rubin, M., C. Koenders, K. Altwegg, M. R. Combi, K.-H. Glassmeier, T. I. Gombosi, K. C. Hansen, U. Motschmann, I. Richter, V. M. Tenishev, and G. Tóth (2014b), Plasma environment of a weak comet - Predictions for Comet 67P/Churyumov-Gerasimenko from multifluid-MHD and Hybrid models, *icarus*, *242*, 38–49, doi:10.1016/j.icarus.2014.07.021.

Rubin, M., X. Jia, K. Altwegg, M. R. Combi, L. K. S. Daldorff, T. I. Gombosi, K. Khurana, M. G. Kivelson, V. M. Tenishev, G. Tóth, B. Holst, and P. Wurz (2015a), Self-consistent multifluid MHD simulations of Europa's exospheric interaction with Jupiter's magnetosphere, *Journal of Geophysical Research (Space Physics)*, *120*, 3503–3524, doi:10.1002/2015JA021149.

Rubin, M., T. I. Gombosi, K. C. Hansen, W.-H. Ip, M. D. Kartalev, C. Koenders, and G. Tóth (2015b), Modeled Interaction of Comet 67P/Churyumov-Gerasimenko with the Solar Wind Inside 2 AU, *Earth Moon and Planets*, doi:10.1007/s11038-015-9476-8.

Russell, C. T., M. A. Saunders, J. L. Phillips, and J. A. Fedder (1986), Near-tail reconnection as the cause of cometary tail disconnections, *J. Geophys. Res.*, , *91*, 1417–1423,

doi:10.1029/JA091iA02p01417.

Schunk, R. W., and A. F. Nagy (2009), *Ionospheres: Physics, Plasma Physics, and Chemistry*, 628 pp.

Shou, Y., M. Combi, Y.-D. Jia, T. Gombosi, G. Toth, and M. Rubin (2015), The Plasma Environment in Comets over a Wide Range of Heliocentric Distances: Application to Comet C/2006 P1 (McNaught), *Astrophys. J.,* , *809*, 156, doi:10.1088/0004-637X/809/2/156.

Siscoe, G. L., G. M. Erickson, B. U. Ö. Sonnerup, N. C. Maynard, J. A. Schoendorf, K. D. Siebert, D. R. Weimer, W. W. White, and G. R. Wilson (2002), Flow-through magnetic reconnection, *Geophys. Res. Lett.,* , *29*, 1626, doi:10.1029/2001GL013536.

Tenishev, V., M. Combi, and B. Davidsson (2008), A Global Kinetic Model for Cometary Comae: The Evolution of the Coma of the Rosetta Target Comet Churyumov-Gerasimenko throughout the Mission, *Astrophys. J.,* , *685*, 659–677, doi:10.1086/590376.

Tóth, G., B. van der Holst, I. V. Sokolov, D. L. De Zeeuw, T. I. Gombosi, F. Fang, W. B. Manchester, X. Meng, D. Najib, K. G. Powell, Q. F. Stout, A. Glocer, Y.-J. Ma, and M. Opher (2012), Adaptive numerical algorithms in space weather modeling, *Journal of Computational Physics*, *231*, 870–903, doi:10.1016/j.jcp.2011.02.006.

Figure 1. The upper panel plots the cometary neutral gas density for Case 1 and the Haser model within 1000 km of the nucleus, while the lower panel shows the cometary neutral gas velocity for Case 1. The vertical dashed lines indicate the inner boundary of the simulation.

Figure 2. The neutral gas distribution in the y=0 plane in the full simulation domain.

Figure 3. The neutral gas distribution in the y=0 (left) and z=0 (right) planes, respectively.

Figure 4. The neutral gas velocity distribution in the y=0 (left) and z=0 (right) planes, respectively.

Figure 5. The cometary heavy ion (H_2O^+) distribution in the y=0 plane in the full simulation domain.

Figure 6. The cometary heavy ion (H_2O^+) distribution within 400 km of the nucleus in the y=0 (left) and z=0 (right) planes, respectively.

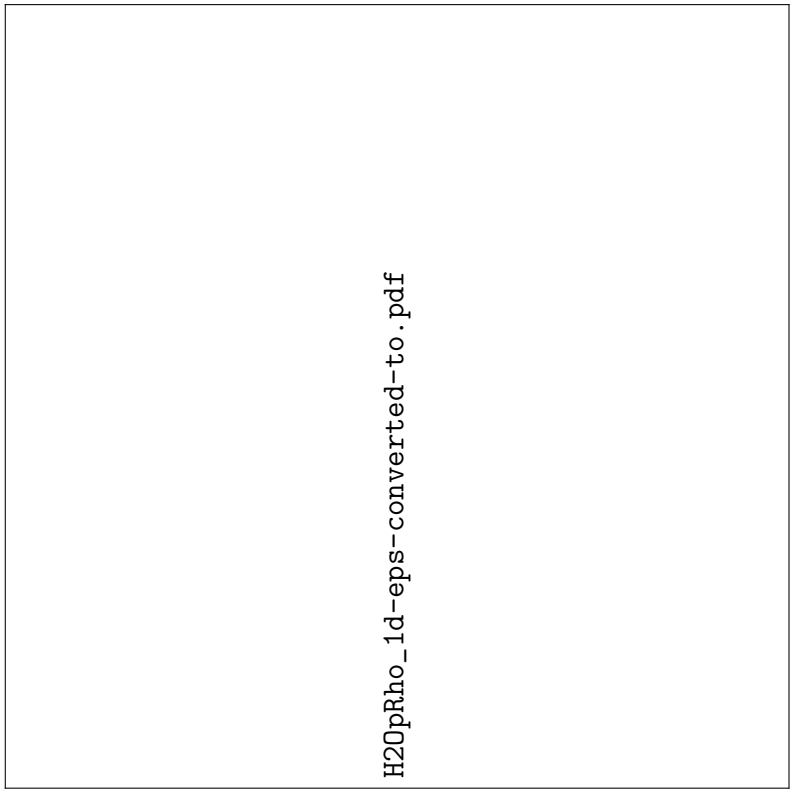

Figure 7. The cometary ion density (solid lines) and solar wind proton density (dashed lines) along the Sun-comet line within 200 km of the nucleus. A density pile up region in both the cometary ion distribution and solar wind proton distribution is located at around 50 km in Case 1 and about 120 km in both Cases 2 and 3 in the +x direction. The pile-up regions in the tail direction is discussed in Section 4.7. The vertical dashed lines indicate the inner boundary of the simulation.

Figure 8. The solar wind proton (H^+) distribution in the y=0 plane in the full simulation domain.

Figure 9. The solar wind proton (H^+) distribution in the y=0 plane within 2×10^4 km in the x-direction of the nucleus. A bow shock is found at around 0.6×10^4 km in Case 1 and about 10^4 km in both Cases 2 and 3.

Figure 10. The magnetic field magnitude within 400 km of the nucleus in the y=0 (left) and z=0 (right) planes, respectively.

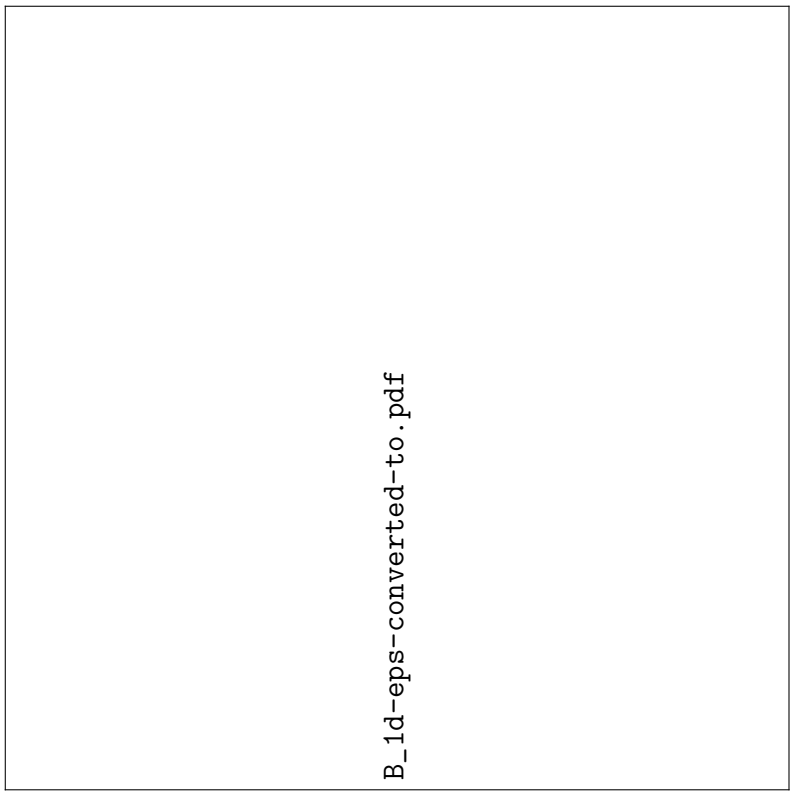

Figure 11. The magnetic field magnitude along the x-axis within 200 km of the nucleus. The vertical dashed lines indicate the inner boundary of the simulation.

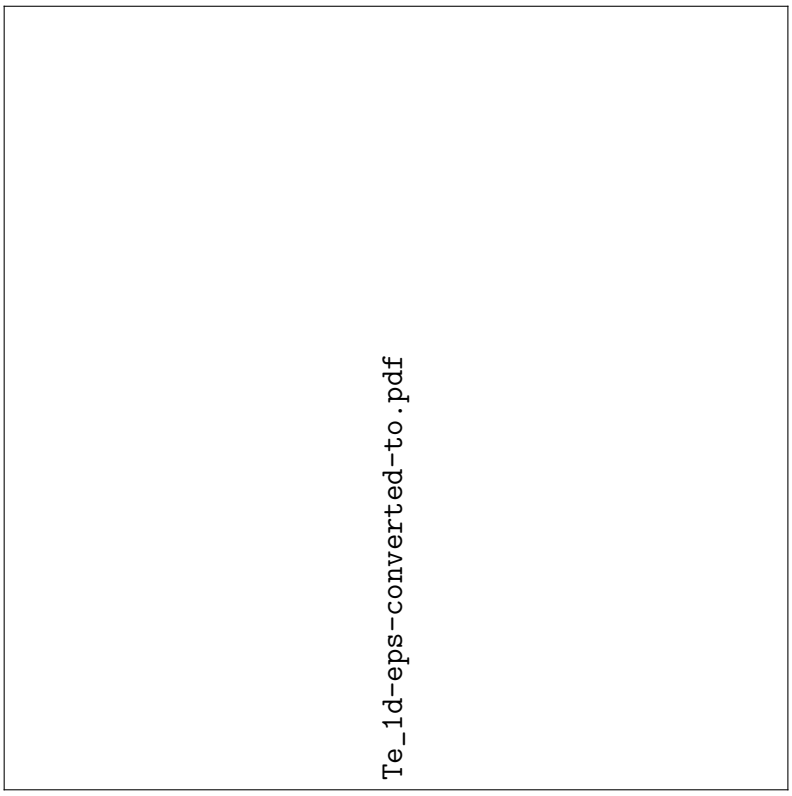

Figure 12. The electron temperature along the Sun-comet line within 200 km of the nucleus. The vertical dashed lines indicate the inner boundary of the simulation.

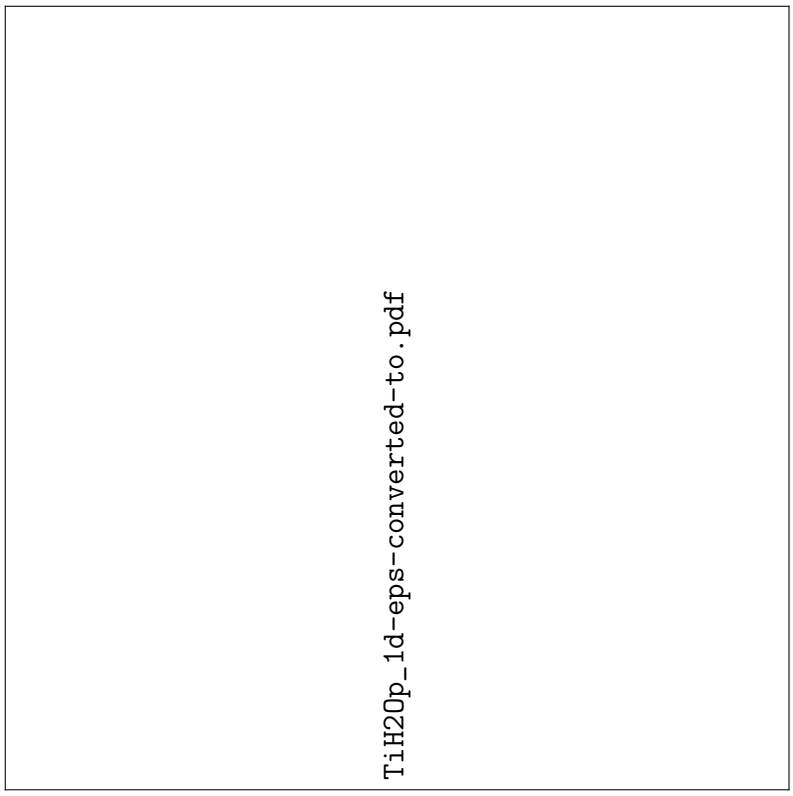

Figure 13. The cometary ion temperature along the Sun-comet line within 200 km of the nucleus. The vertical dashed lines indicate the inner boundary of the simulation.

Figure 14. Left panels show the magnetic field strength with its direction vectors in the z=0 plane in the tail region for the three cases. Right panels plot the cometary ion density with their velocity vectors in the z=0 plane.

Figure 15. The cometary ion density with their velocity vectors in the y=0 plane in the tail region.

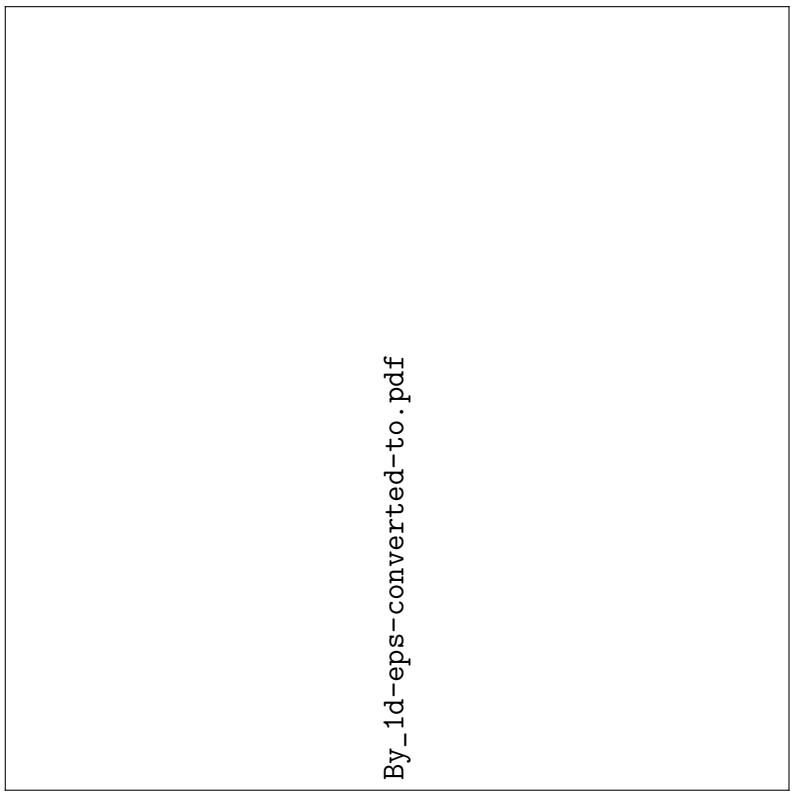

Figure 16. The B_y component along the Sun-comet line. The vertical dashed lines indicate the inner boundary of the simulation. The horizontal dashed line indicates the value of zero.

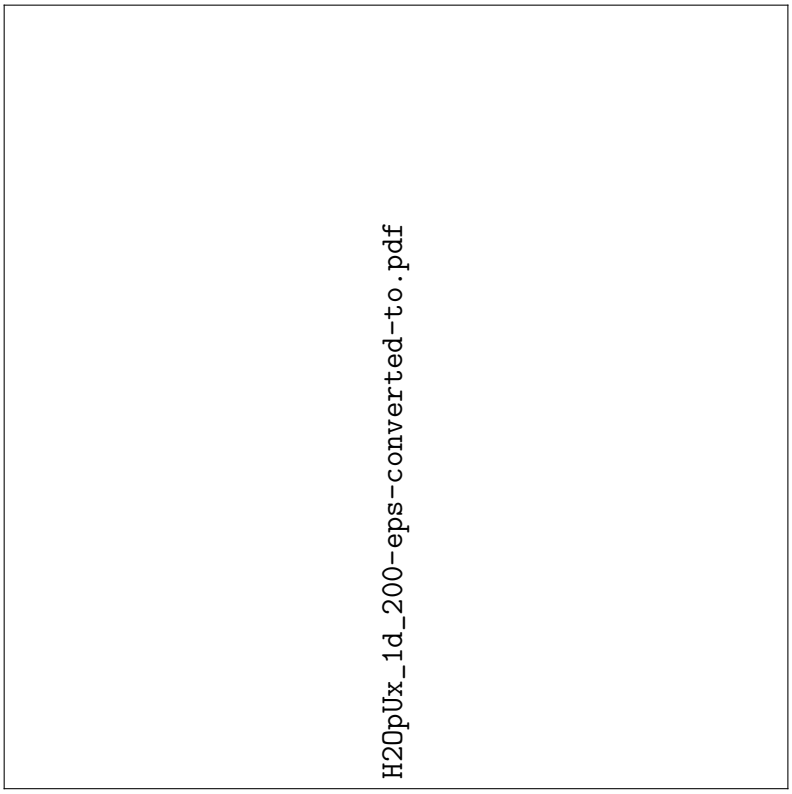

Figure 17. The cometary ion V_x component along the Sun-comet line. The vertical dashed lines indicate the inner boundary of the simulation. The horizontal dashed line indicates the value of zero.

Elastic collision rates	Value [m^3s^{-1}]
Ion-ion	$1.27 \cdot 10^{-6} \frac{Z_s^2 Z_t^2 \sqrt{m_{st}}}{m_s} \frac{n_t}{T^{3/2}}$
Ion-neutral	$10^{-6} C_{sn} n_n$
Electron-ion	$54.5 \cdot 10^{-6} \frac{n_s Z_s^2}{T_e^{3/2}}$
Ion-electron	$1.27 \cdot 10^{-6} \frac{\sqrt{m_e}}{m_s} \frac{n_e Z_s^2}{T_e^{3/2}}$
Electron-water	$2.745 \cdot 10^{-11} n_n T_e^{-0.62}$

Table 1. The elastic collision rates are taken from *Schunk and Nagy* [2009] except the electron-water elastic collision rate is taken from *Itikawa* [1971]. Z_s and Z_t are the charge states of the ion species s and t, m_s and m_t are the atomic masses of species s and t in [amu], $m_{st} = \frac{m_s m_t}{m_s + m_t}$ (m_t is the atomic mass of the species t in [amu]) is the reduced mass in [amu], m_e is the electron mass in [amu], n_t and n_s are the number densities of the species t and s in [m^{-3}], n_n is the neutral gas number density in [m^{-3}], $T_{st} = \frac{m_s T_t + m_t T_s}{m_s + m_t}$ (T_s and T_t are the temperatures for the ion species s and t in [K]) is the reduced temperature in [K]. C_{sn} are numerical coefficients obtained from *Schunk and Nagy* [2009]. Both the H_2O^+-electron and H^+-electron recombination rates are taken from *Schunk and Nagy* [2009].

	$F_{\min}$ [m^{-2} s^{-1}]	$F_{\max}$ [m^{-2} s^{-1}]	$T_{\min}$ [K]	$T_{\max}$ [K]	ΔT [K]
Case 1	$1.56 \cdot 10^{20}$	$1.56 \cdot 10^{20}$	170.7	170.7	0
Case 2	$9.02 \cdot 10^{18}$	$6.60 \cdot 10^{20}$	140.0	195.97	2.47
Case 3	$1.17 \cdot 10^{19}$	$8.61 \cdot 10^{20}$	140.0	195.97	2.47

Table 2. The parameters for the flux and temperature approximation.

Parameter	Value
Distance to the Sun	1.3 AU
Gas production rate	$8 \cdot 10^{27}$ s^{-1}
Photo-ionization frequency	$6 \cdot 10^{-7}$ s^{-1}
Solar wind velocity	400 km/s
Solar wind density	6 protons/cm^3
Solar wind ion temperature	$7.9 \cdot 10^4$ K
Solar wind electron temperature	$1.3 \cdot 10^5$ K
Interplanetary magnetic field B_y component	4.8 nT

Table 3. The input parameters for the model. The photo-ionization frequency is scaled from the nominal value at 1 AU from *Hansen et al.* [2007] (also see *Rubin et al.* [2015b]).

	Bow shock distance [km]	diamagnetic cavity distance [km]
Case 1	6000	50
Case 2	10,000	100
Case 3	10,000	100

Table 4. The distances of the bow shock and the diamagnetic cavity boundary. The distances are given from the center of the nucleus along the +x axis.

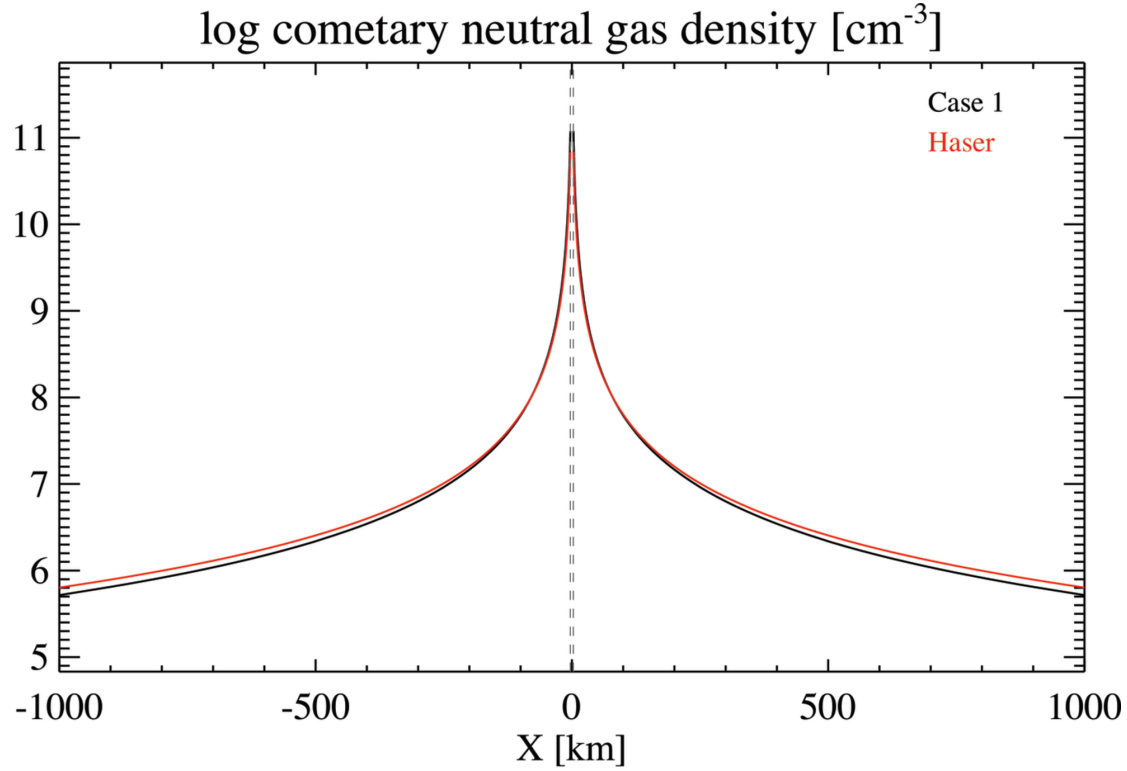

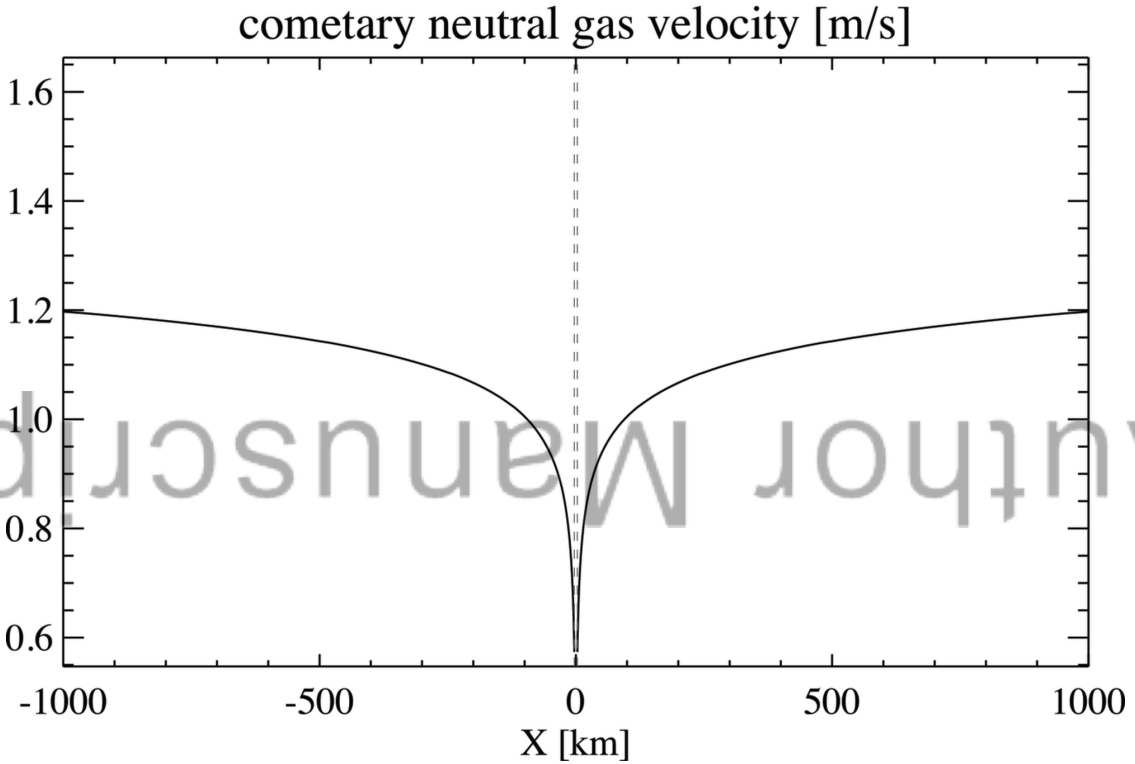

2015ja022333-f01-z-

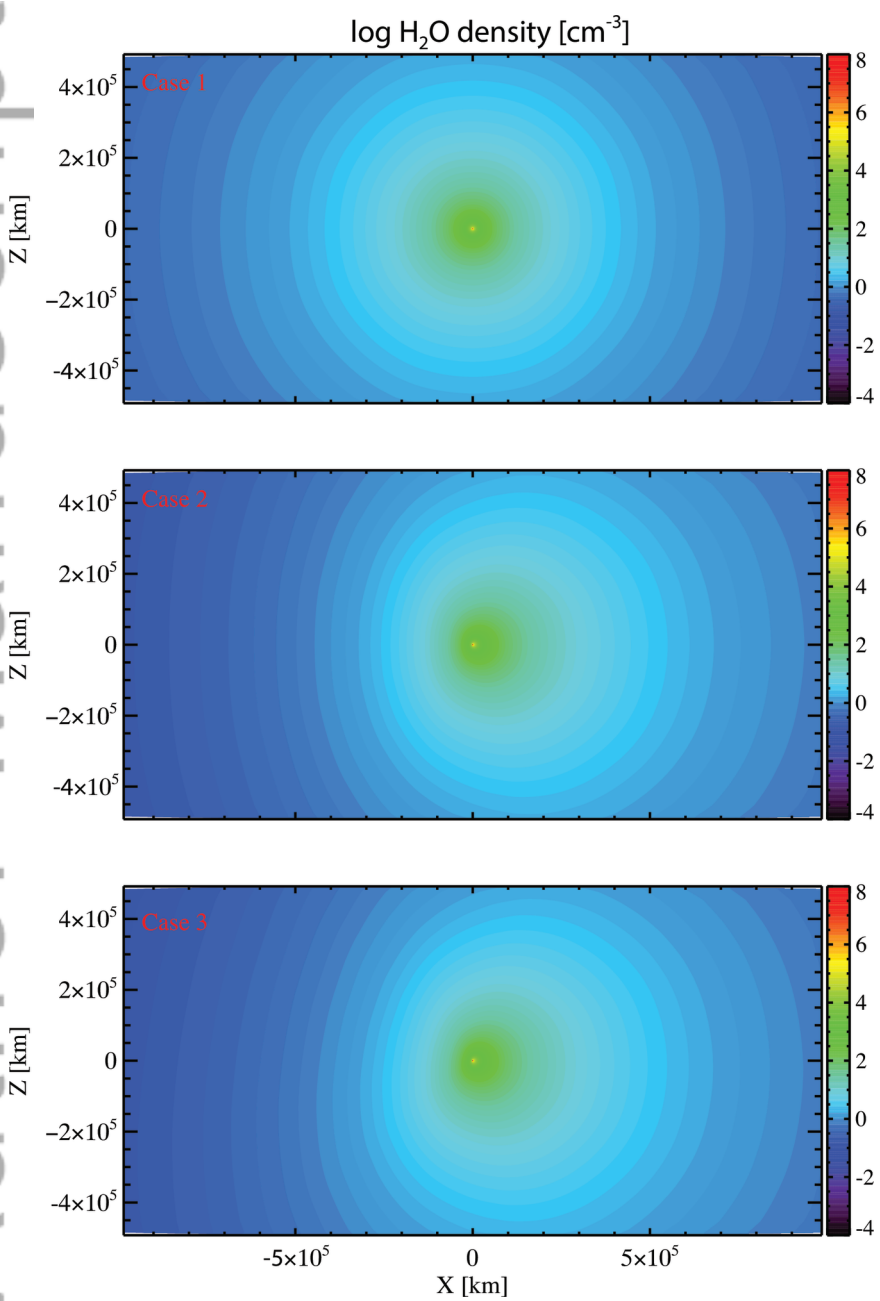

2015ja022333-f02-z-

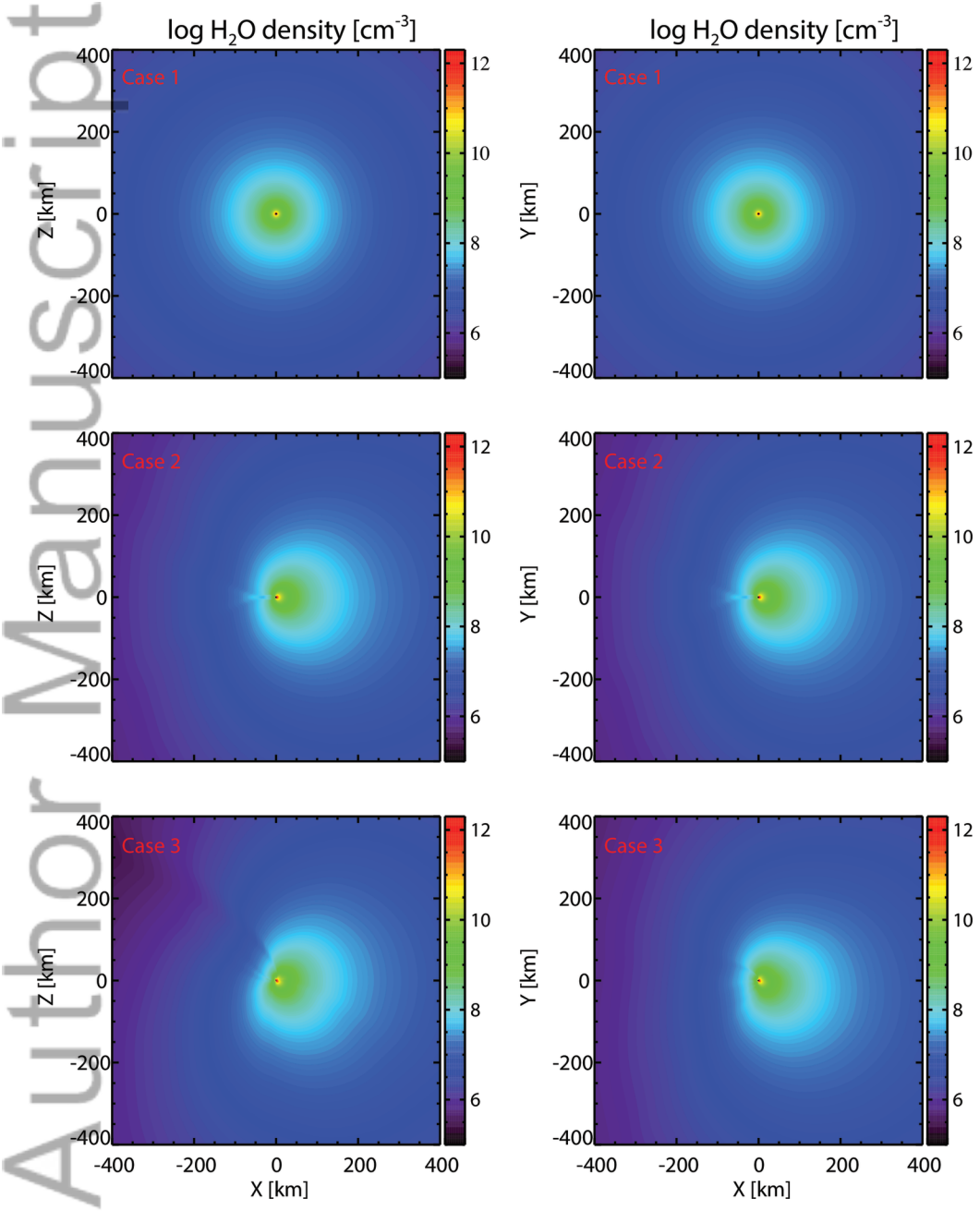

2015ja022333-f03-z-

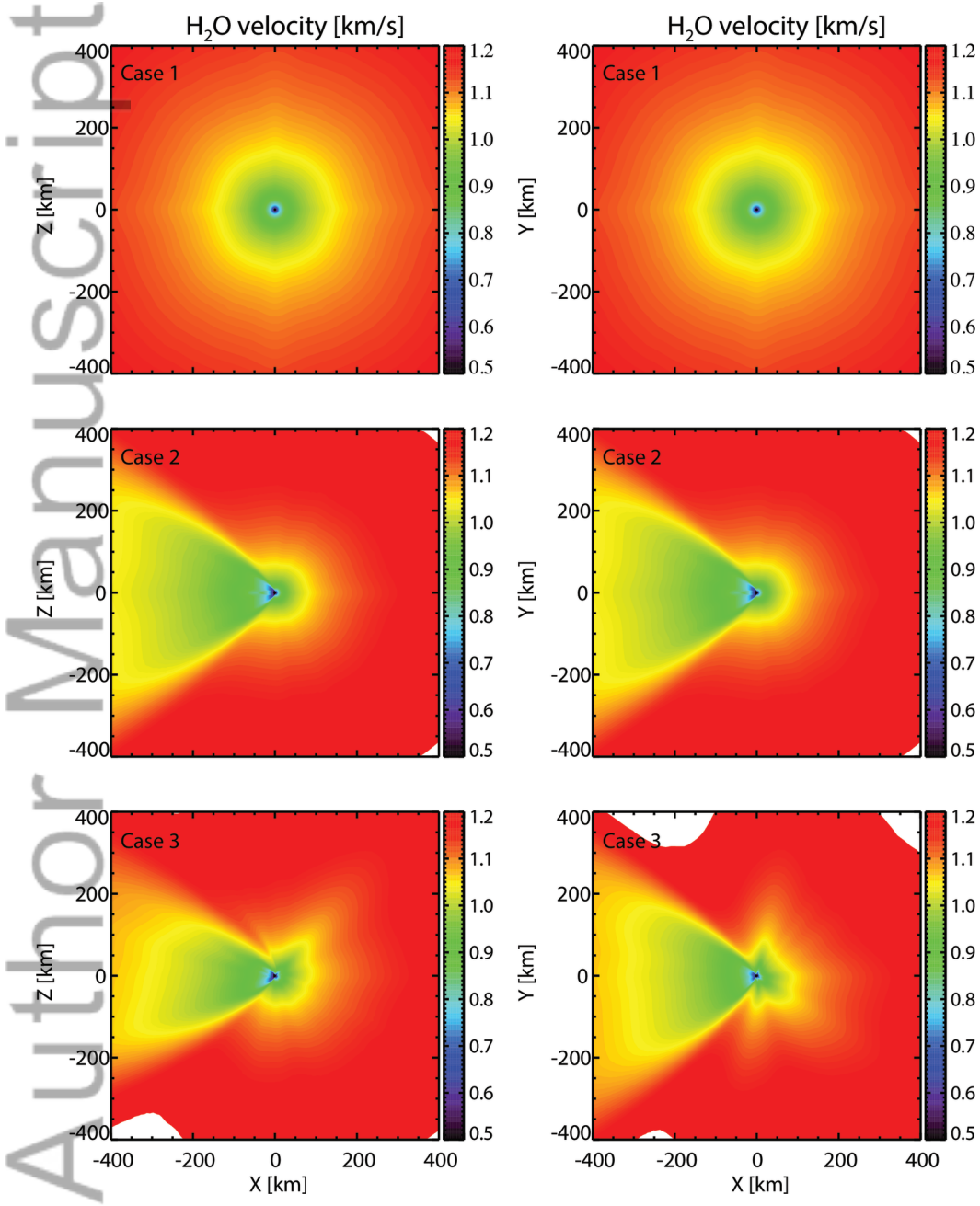

2015ja022333-f04-z-

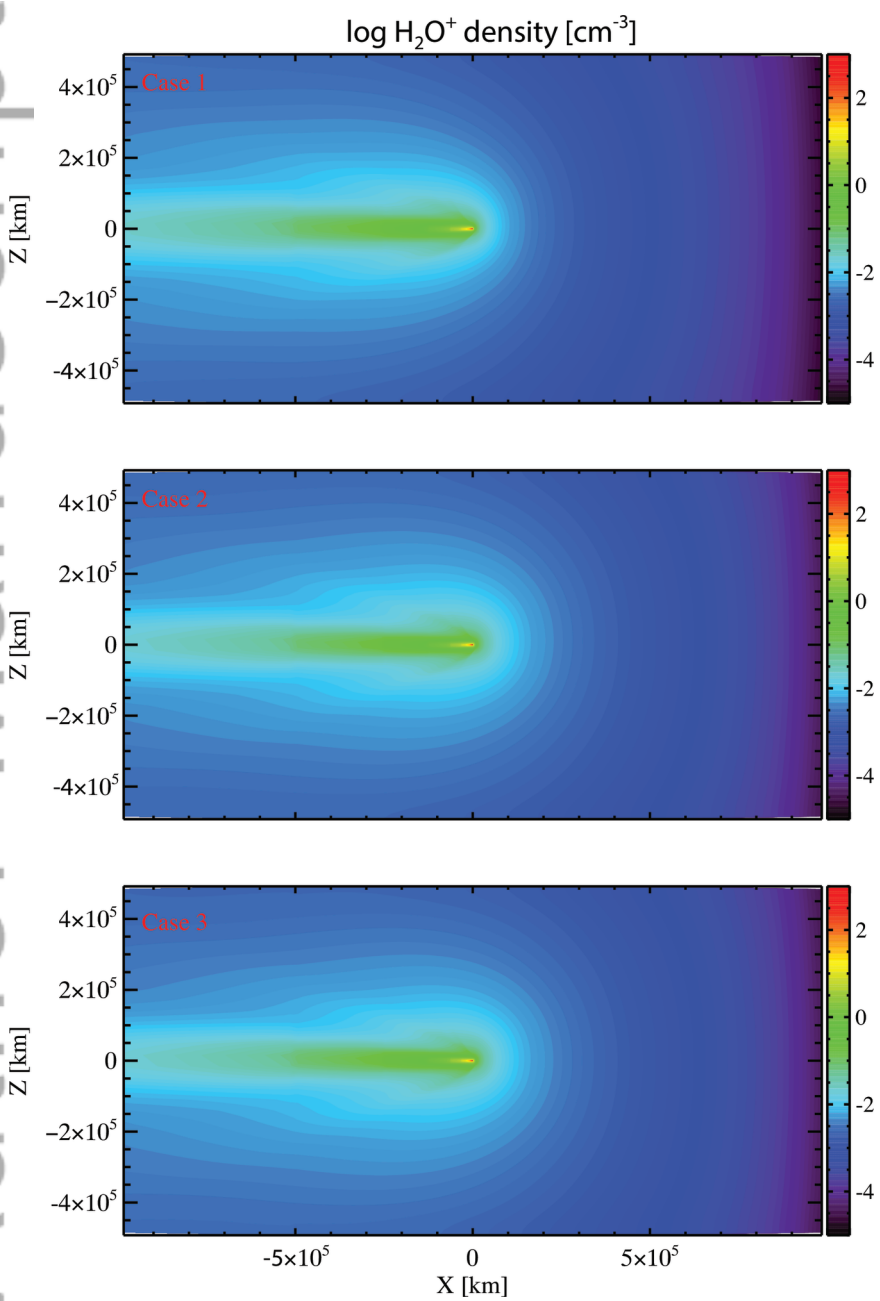

2015ja022333-f05-z-

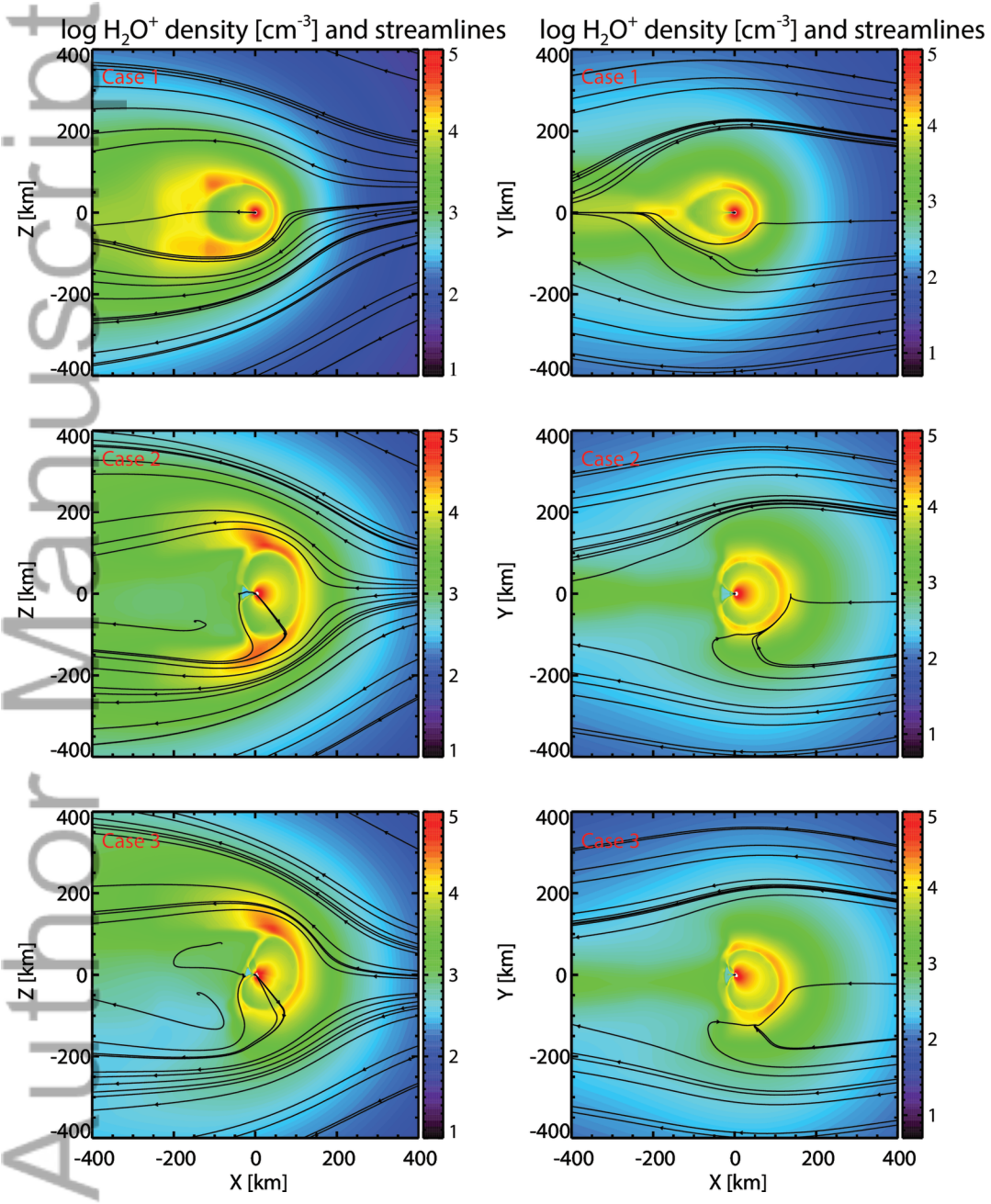

2015ja022333-f06-z-

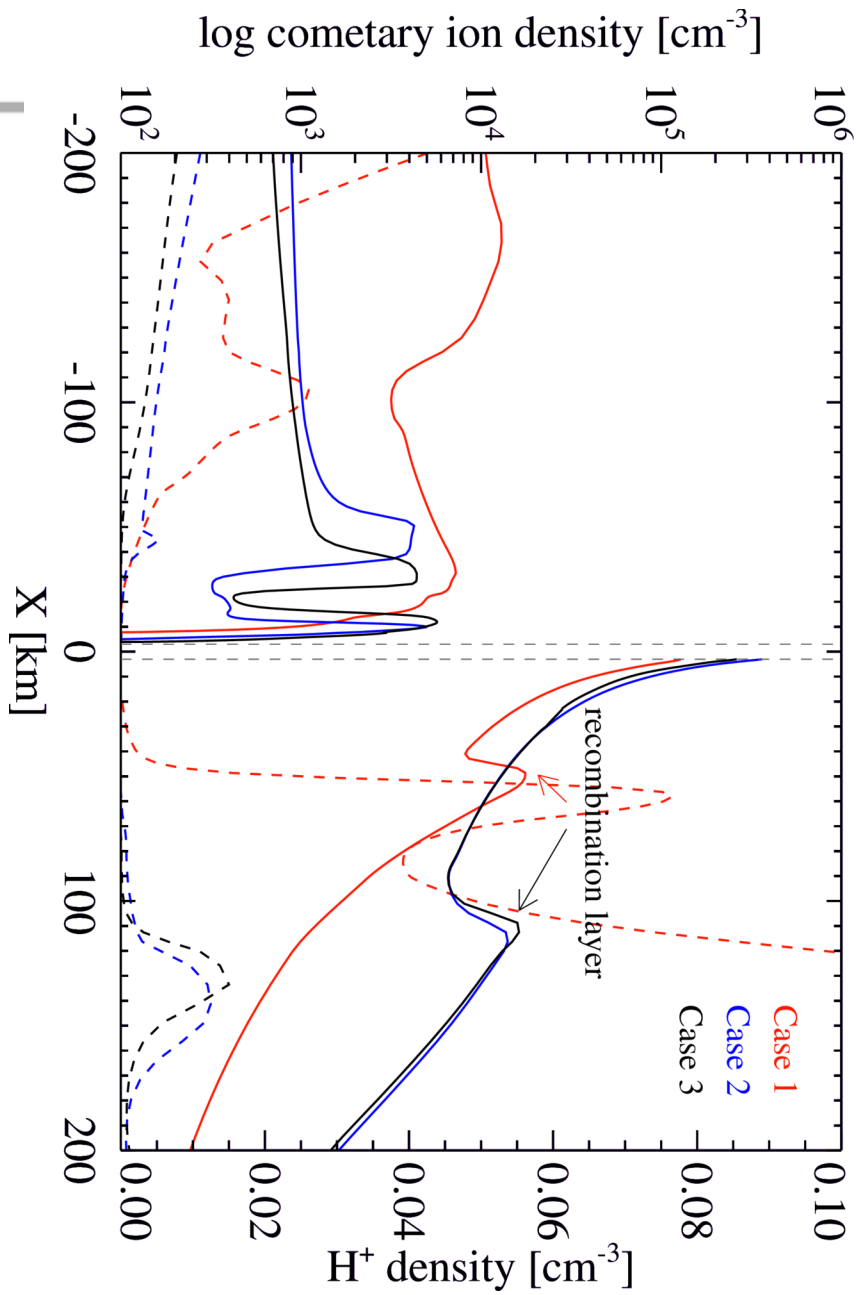

2015ja022333-f07-z-

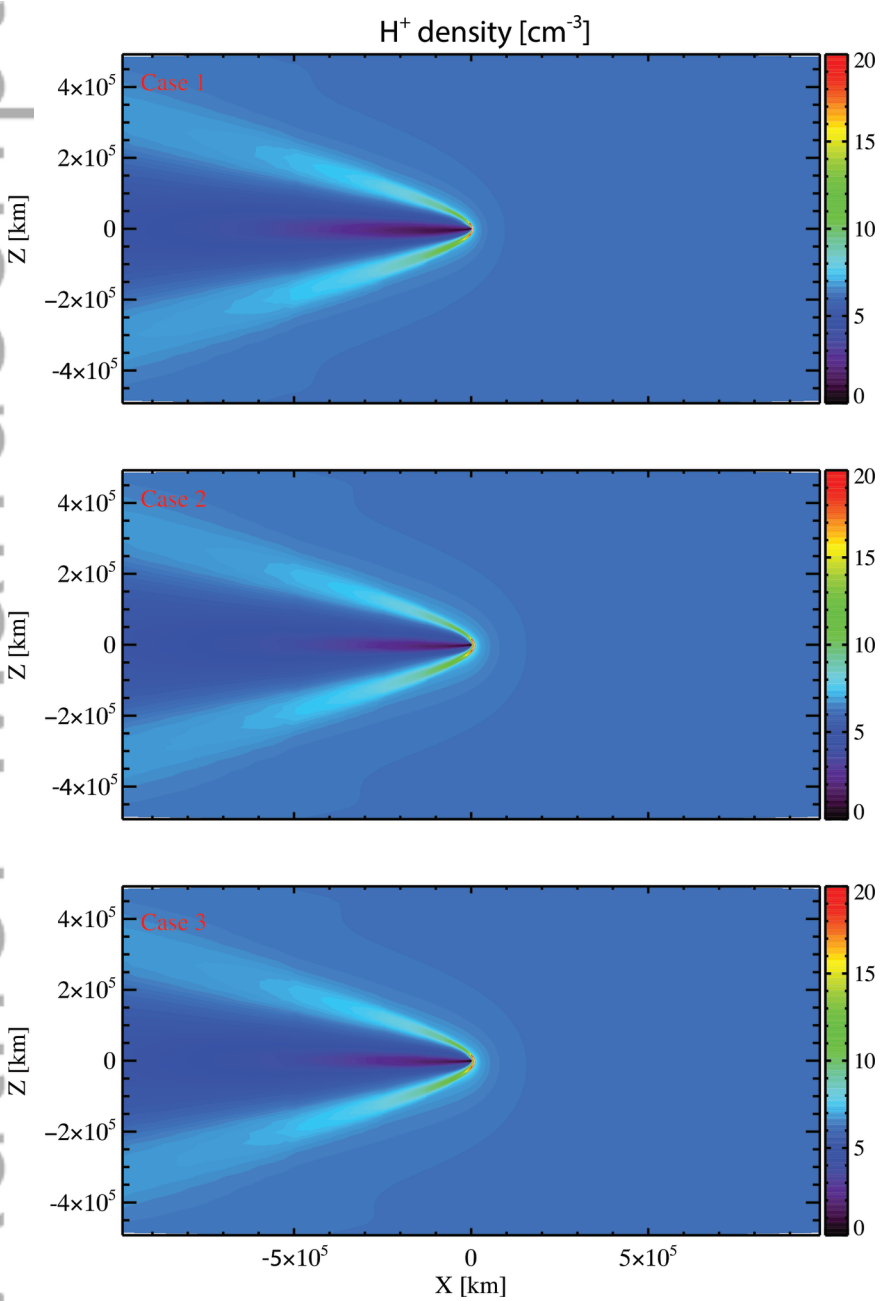

2015ja022333-f08-z-

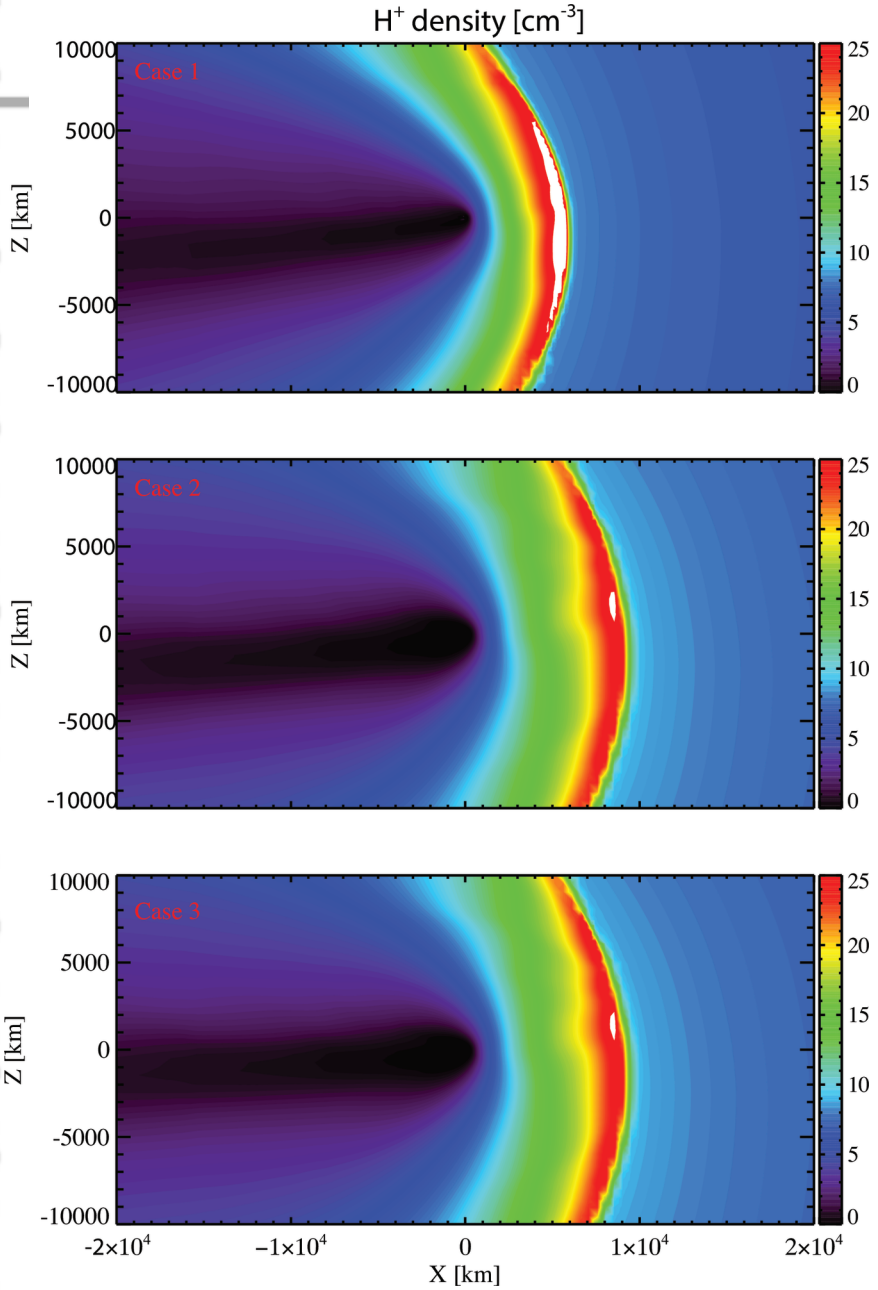

2015ja022333-f09-z-

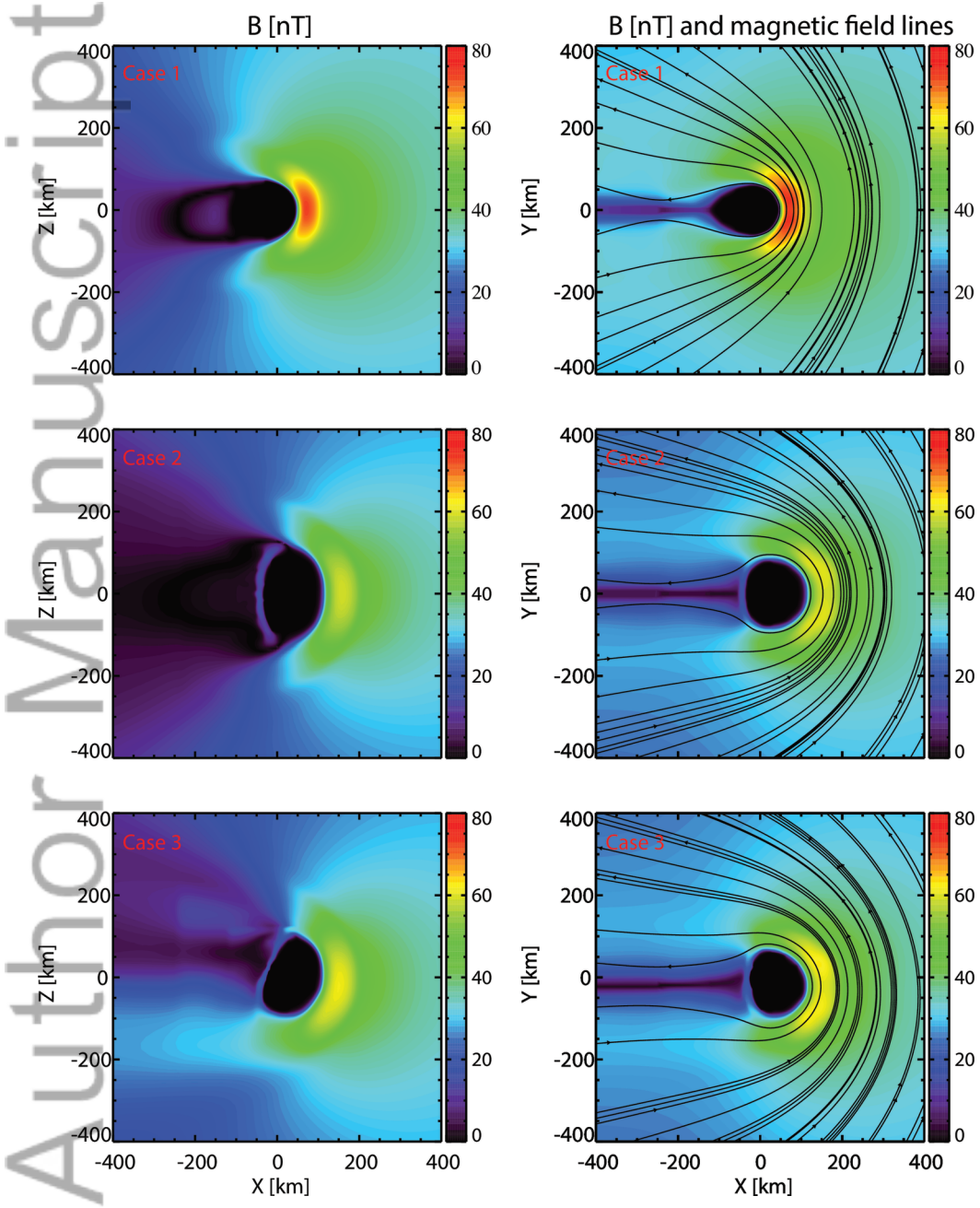

2015ja022333-f10-z-

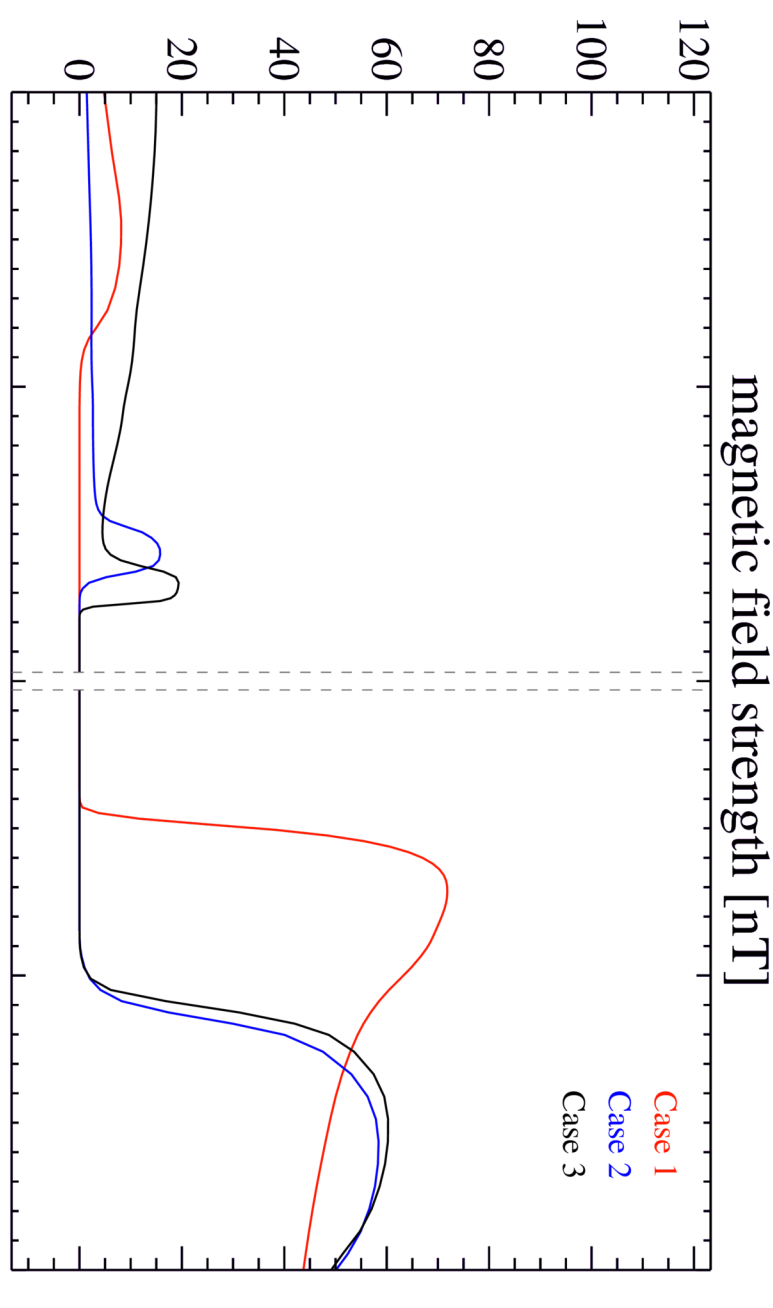

2015ja022333-f11-z-

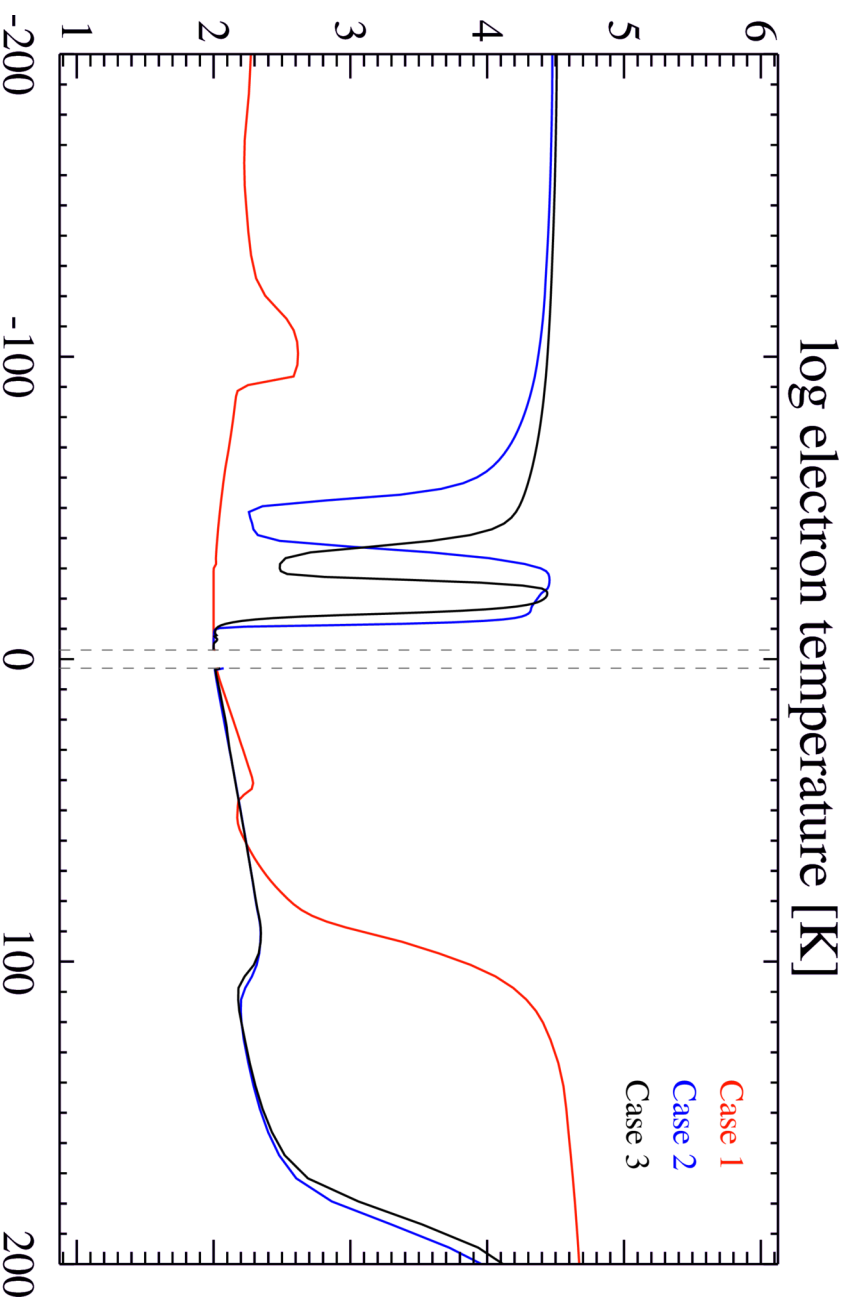

2015ja022333-f12-z-

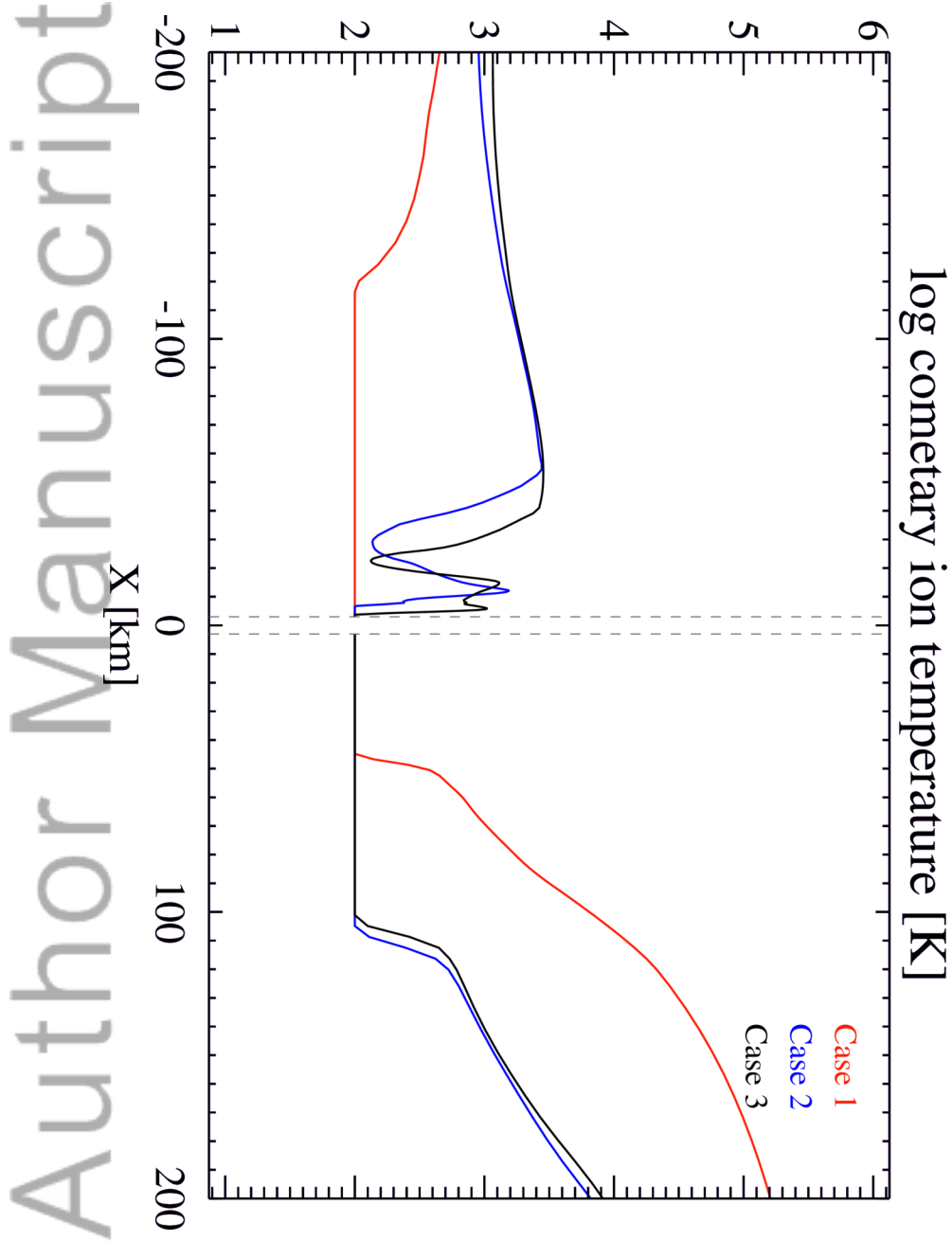

2015ja022333-f13-z-

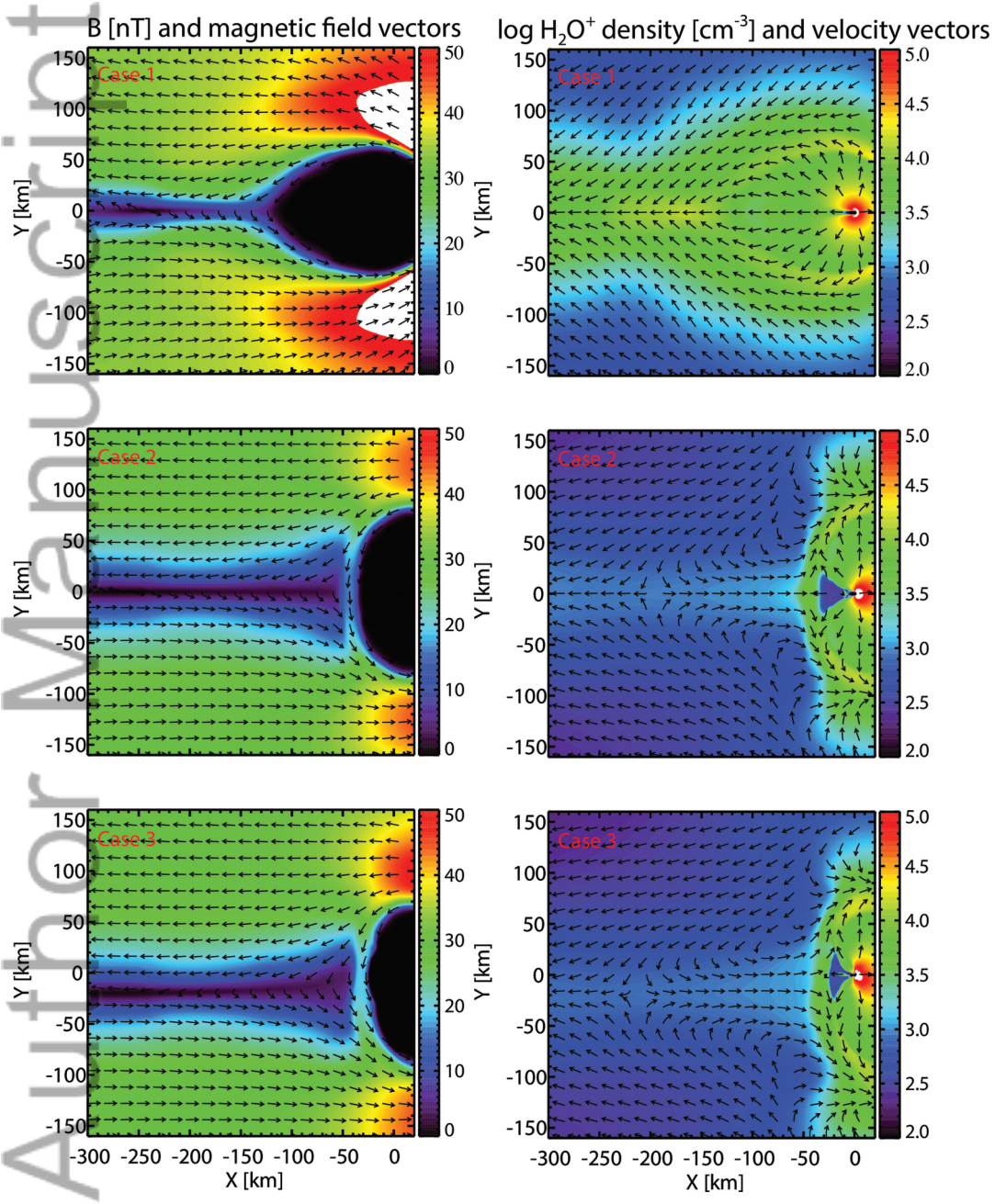

2015ja022333-f14-z-

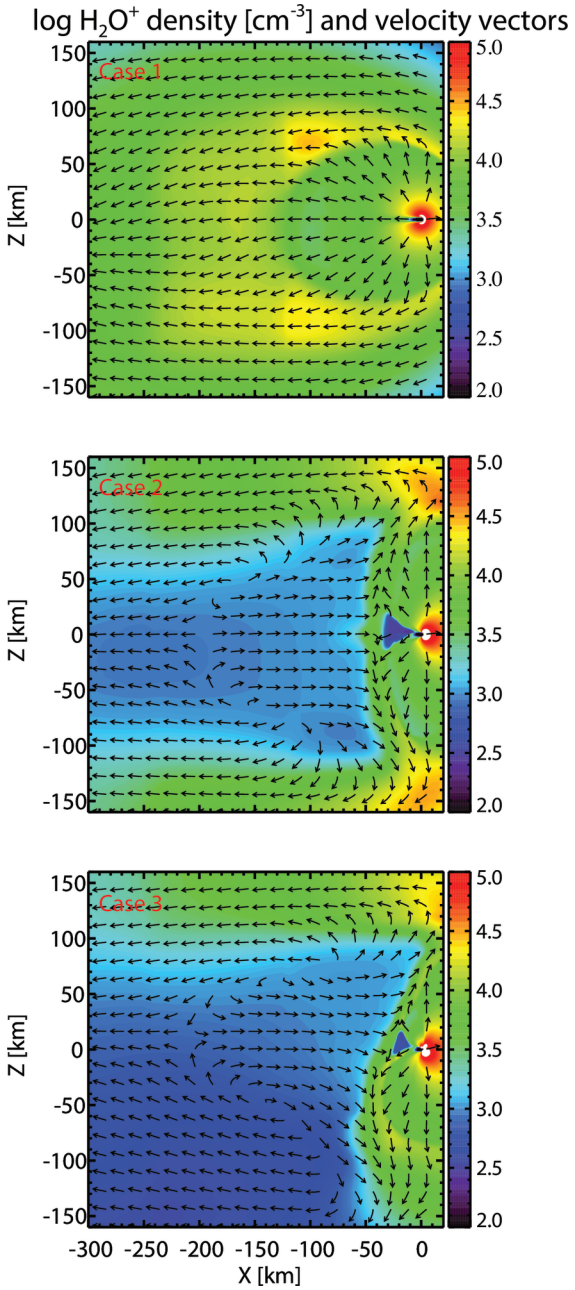

2015ja022333-f15-z-

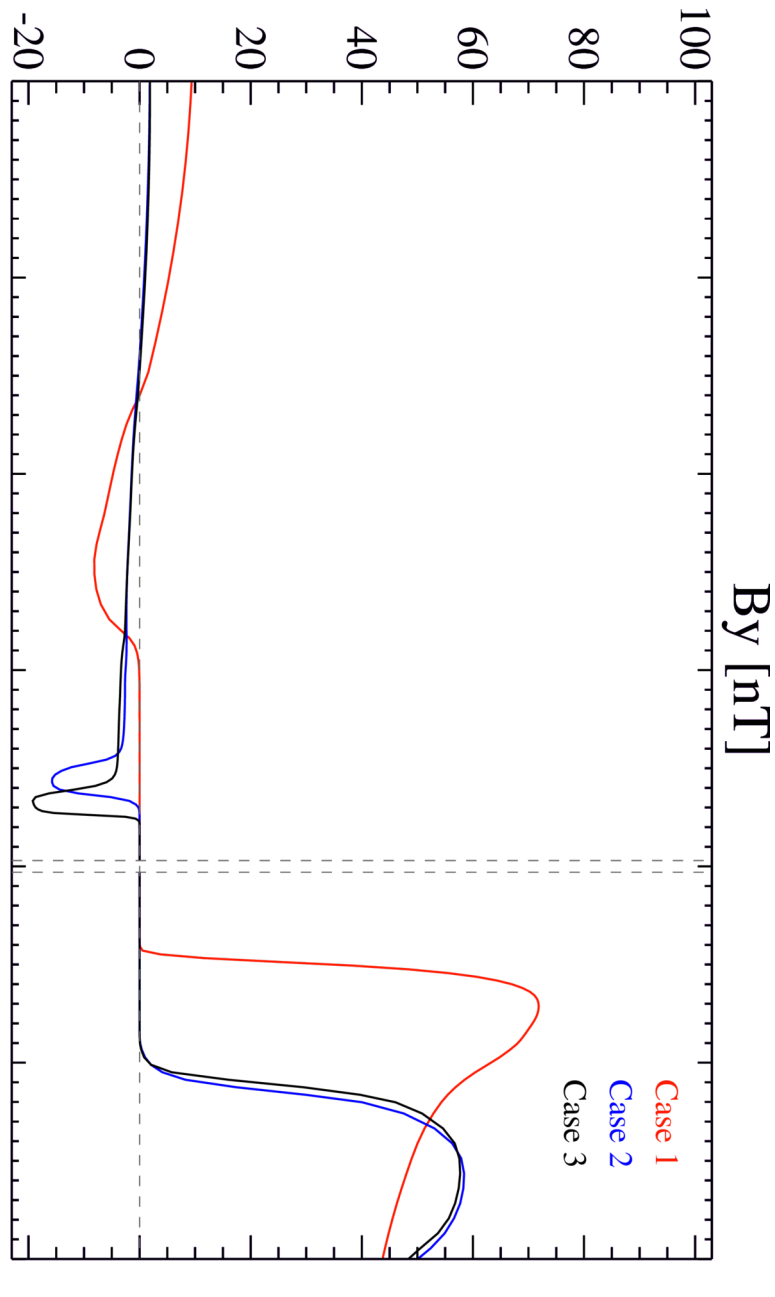

2015ja022333-f16-z-

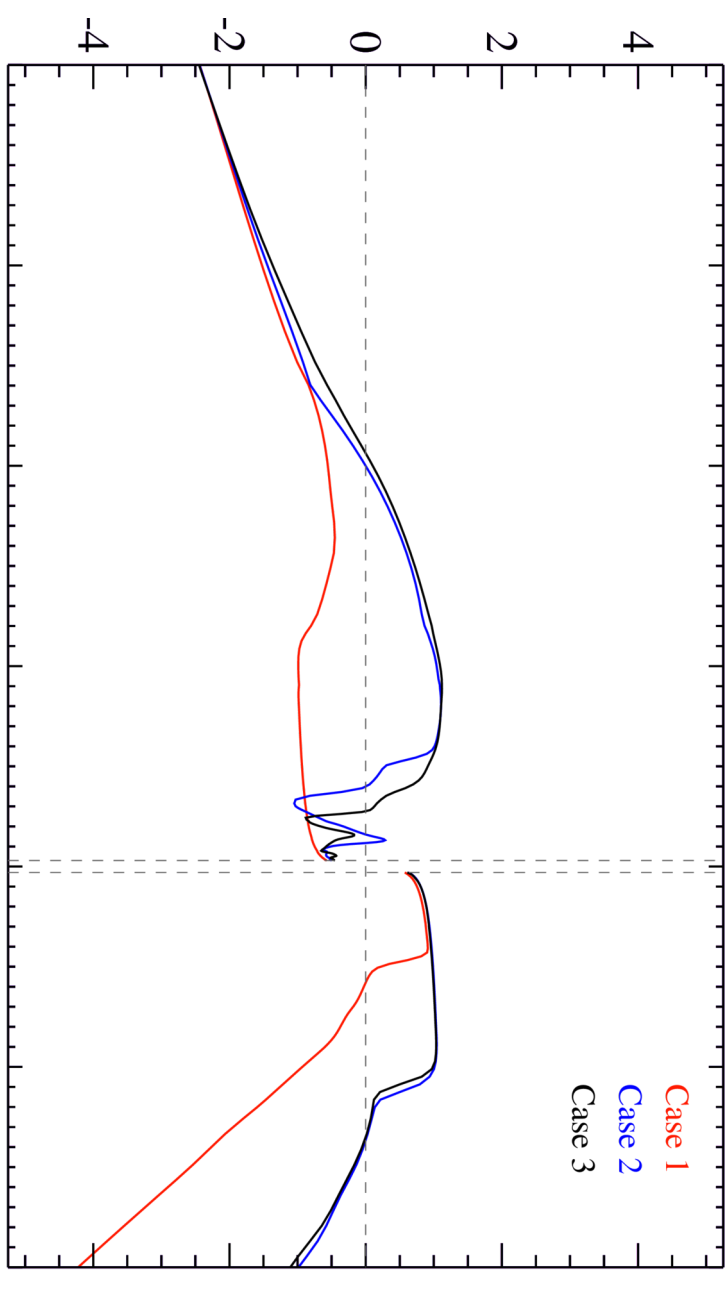

2015ja022333-f17-z-